STEM CELLS®

TISSUE-SPECIFIC STEM CELLS

Endogenous Mesenchymal Stromal Cells in Bone Marrow Are Required to Preserve Muscle Function in mdx Mice

RYO FUJITA,[a] KATSUTO TAMAI,[b] ERIKO AIKAWA,[b] KEISUKE NIMURA,[a] SAKI ISHINO,[c] YASUSHI KIKUCHI,[b] YASUFUMI KANEDA[a]

Key Words. Mesenchymal stromal cells • Duchenne muscular dystrophy • TNF-α-stimulated gene/protein-6 • TSG-6 • Muscle satellite cells • Bone marrow cells

[a]Division of Gene Therapy Science, [b]Department of Stem Cell Therapy Science, and [c]Center for Medical Research and Education, Graduate School of Medicine, Osaka University, Osaka, Japan

Correspondence: Katsuto Tamai, M.D., Ph.D., Department of Stem Cell Therapy Science, Graduate School of Medicine, Osaka University, 2-2, Yamada-oka, Suita, Osaka 565-0871, Japan. Telephone: 81-6-6879-3901; Fax: 81-6-6879-3909; e-mail: tamai@gts.med.osaka-u.ac.jp; or Yasufumi Kaneda, M.D., Ph.D., Division of Gene Therapy Science, Graduate School of Medicine, Osaka University, 2-2, Yamada-oka, Suita, Osaka 565-0871, Japan. Telephone: 81-6-6879-3901; Fax: 81-6-6879-3909; e-mail: kaneday@gts.med.osak-u.ac.jp

Received July 9, 2014; accepted for publication October 31, 2014; first published online in STEM CELLS *EXPRESS* November 19, 2014.

1066-5099/2014/$30.00/0

http://dx.doi.org/10.1002/stem.1900

ABSTRACT

The physiological role of "endogenous" bone marrow (BM) mesenchymal stromal cells (MSCs) in tissue regeneration is poorly understood. Here, we show the significant contribution of unique endogenous BM-MSC populations to muscle regeneration in Duchenne muscular dystrophy (DMD) mice (mdx). Transplantation of BM cells (BMCs) from 10-week-old mdx into 3–4-week-old mdx mice increased inflammation and fibrosis and reduced muscle function compared with mdx mice that received BMCs from 10-week-old wild-type mice, suggesting that the alteration of BMC populations in mdx mice affects the progression of muscle pathology. Two distinct MSC populations in BM, that is, hematopoietic lineage (Lin)$^-$/ckit$^-$/CD106$^+$/CD44$^+$ and Lin$^-$/ckit$^-$/CD106$^+$/CD44$^-$ cells, were significantly reduced in 10-week-old mdx mice in disease progression. The results of a whole-transcriptome analysis indicated that these two MSC populations have distinct gene expression profiles, indicating that the Lin$^-$/ckit$^-$/CD106$^+$/CD44$^+$ and Lin$^-$/ckit$^-$/CD106$^+$/CD44$^-$ MSC populations are proliferative- and dormant-state populations in BM, respectively. BM-derived Lin$^-$/CD106$^+$/CD44$^+$ MSCs abundantly migrated to damaged muscles and highly expressed tumor necrosis factor-alpha-stimulated gene/protein-6 (TSG-6), an anti-inflammatory protein, in damaged muscles. We also demonstrated that TSG-6 stimulated myoblast proliferation. The injection of Lin$^-$/ckit$^-$/CD106$^+$/CD44$^+$ MSCs into the muscle of mdx mice successfully ameliorated muscle dysfunction by decreasing inflammation and enhancing muscle regeneration through TSG-6-mediated activities. Thus, we propose a novel function of the unique endogenous BM-MSC population, which countered muscle pathology progression in a DMD model. STEM CELLS *2015;33:962–975*

INTRODUCTION

Bone marrow (BM) is a source of hematopoietic stem cells (HSCs) and also contains nonhematopoietic stromal cell populations known as mesenchymal stromal cells (MSCs). Conventionally, MSCs have been defined as colony-forming unit-fibroblasts (CFU-Fs) with the capacity to differentiate into adipocytes, chondrocytes, and osteocytes in vitro [1, 2]. Culture-expanded MSCs have been used to treat various tissue injuries, such as myocardial infarction and lung and skin injuries [3–5]. A focus of great interest regarding the use of culture-expanded MSCs in clinical applications is their anti-inflammatory and regeneration activities, which render the microenvironment more efficient for promoting tissue regeneration [3, 6].

Our previous studies revealed that, similar to culture-expanded BM-MSCs, circulating BM-derived osteoblast progenitor cells were attracted by bone morphogenetic protein-2 to contribute to ectopic bone formation [7, 8]. We also found previously that necrotic skin-derived high-mobility group box 1 (HMGB1) mobilizes platelet-derived growth factor receptor alpha-positive (PDGFRα$^+$) mesenchymal cells from the BM into circulation [9]. These data suggest that injury stimuli attract endogenous BM-MSC populations via the circulation to support tissue regeneration.

However, the characteristics of these endogenous BM-MSC populations mobilized from BM into circulation and damaged tissues have not been established because of their low number and high heterogeneity. In addition, another endogenous function of MSCs in BM is to maintain HSC quality and quantity as a niche by secreting stem cell factor and/or C-X-C type chemokine ligand 12 (CXCL12), known as stromal cell-derived factor 1α (SDF-1α)

[10–14]. Together, the results of our previous investigations along with those of other seminal studies suggest that multiple MSC populations exist in BM, possibly with distinct functions, such as supporting HSCs and contributing to tissue regeneration [15, 16].

Although information regarding the functions and surface markers of culture-expanded MSCs has accumulated, the molecular characteristics of endogenous BM-MSCs are still poorly understood [17, 18]. It is thus necessary to explore BM-MSC populations contributing to the tissue regeneration processes and their molecular signatures —such as gene expression profiles—to elucidate the specific functions of each MSC population in vivo. In previous research, we investigated the dynamics of BM-MSCs in acute injury and regeneration models [8, 9], but it remains unclear whether endogenous BM-MSCs also support tissue regeneration in chronic tissue damage and regeneration processes, such as those in Duchenne muscular dystrophy (DMD).

DMD is characterized primarily by progressive muscle degeneration and weakness due to mutations in the dystrophin gene [19–21]. Muscle cells without dystrophin are vulnerable to damage, resulting in cycles of degeneration and regeneration, chronic inflammation, severe fibrosis, and reduced muscle contractility. Currently, therapies for DMD can be divided into two groups: treatments targeting the restoration of dystrophin expression by cell therapies [22–26] and treatments for tilting the balance of overall muscle condition in favor of regeneration by the activation of satellite cells and the suppression of inflammation and fibrosis [27, 28]. However, there is no curative treatment for DMD at present.

In addition to these therapies, boosting endogenous muscle repair mechanisms is an alternative and feasible approach to treat muscle diseases. In light of the accumulated findings, the activation of muscle repair mechanisms by endogenous BM-MSCs could be an attractive novel approach to slow the progression of muscle dysfunction in DMD. For this purpose, a better understanding of the roles of endogenous BM-MSCs in the pathology of DMD as well as the identification of endogenous molecular characteristics in vivo is urgently required.

In this study, we investigated the contribution of "endogenous" BM-MSCs to muscle regeneration in a DMD mouse model (mdx). Using a bone marrow transplantation (BMT) model, we found that alterations of the endogenous BM-MSC population affect the muscle pathological conditions in mdx mice. In an evaluation of an endogenous BM-MSC population by a whole-genome transcriptome analysis and flow cytometry analysis, we characterized the heterogeneity of endogenous BM-MSCs and identified the dominantly recruited BM-MSC population into damaged muscles in mdx mice. The treatment of this specific BM-MSC population alone stimulated the muscle regeneration processes. We believe that these findings provide new insight into muscle repair mechanisms with specific endogenous BM-MSC populations, and our results contribute to the understanding of BM-MSC-mediated muscle repair mechanisms that can slow disease progression in DMD.

Materials and Methods

Mice

All animals were handled according to approved protocols and the guidelines of the Animal Committee of the Osaka University Graduate School of Medicine. C57BL/6, C57BL/10ScSn/J, and C57BL/10ScSn-Dmd^{mdx}/J (referred to as mdx) mice were purchased from CLEA Japan (Tokyo). C57BL/6 mice that ubiquitously expressed enhanced green fluorescent protein (GFP, referred to as GFP mice) were kindly provided by Masaru Okabe (Osaka University, Osaka, Japan). B6.129S4-Pdgfra$^{tm11(EGFP)Sor}$/J mice (referred to as PDGFRα-H2BGFP) were purchased from The Jackson Laboratory (West Grove, PA). PDGFRα-H2BGFP mice were heterozygous knockin mice in which the histone H2B-GFP fusion gene was inserted into the locus of the PDGFRα gene.

Muscle Endurance Test and Grip-Strength Test

To determine the muscle endurance in mice, a mouse was allowed to grasp the bar or metallic mesh and remain suspended (Supporting Information Fig. S1F, S1G). The time until the mouse released its grip was recorded. Each mouse was subjected to six tests, and the results from these tests were averaged. The final outcome value for the muscle endurance was determined using the holding impulse (second × body weight, g) to correct for the negative effects of body mass on the hang time. The whole-limb grip strength was measured using a Grip Strength Meter for mice (Muromachi Kikai, Tokyo). The mouse was allowed to grasp a horizontal mesh platform with all four limbs, and then, the mouse's tail was pulled back parallel to the mesh platform. The peak tension (gram; g) was recorded when the mouse released its grip. Six sets of measurements were performed for each mouse, and the average values were defined as the mouse whole-limb grip strength.

Isolation of Bone Marrow Cells and Bone Marrow Transplantation

The isolation of BM cells (BMCs) and BMT was performed as described [7, 9]. Briefly, under sterile conditions, BMCs were isolated by flushing the femurs and tibiae with 2% fetal bovine serum (FBS)/phosphate-buffered saline (PBS). For the total BMT, 5×10^6 BMCs were injected into the tail veins of mice irradiated with 10 Gy. Six weeks after reconstitution, the chimerisms were examined, and the results confirmed that more than 90% of the total BMCs were donor-derived cells (Supporting Information Fig. S2A, S2B). For the preparation of each mouse with reduced MSCs in BM, GFP$^+$/Lin$^-$/ckit$^+$ BMCs, which include HSC but not MSC populations, were sorted with the FACSAria II cell sorter (BD Biosciences, San Jose, CA; Supporting Information Fig. S3A). Each irradiated mouse received $1 \times 10^5 - 2 \times 10^5$ GFP$^+$/Lin$^-$/ckit$^+$ BMCs, the number of which was almost identical to that of the GFP$^+$/Lin$^-$/ckit$^+$ BMCs for the total BMT. After reconstitution, the numbers and percentages of donor-derived-MSC populations in BM were examined (Supporting Information Fig. S3B–S3F).

Preparation of Conditioned Media

For the preparation of conditioned media, culture-expanded BM-MSCs at passage 3 were used. The BM-MSCs were stimulated with 10% wild-type (WT) or mdx mouse serum for 2 days. The medium was then changed to fresh α-MEM, and another 2 days of incubation was performed. The conditioned media of these cells were collected and used to stimulate C2C12 cells.

Isolation of Primary Satellite Cells and C2C12 Cells

For the isolation of single myofibers, the extensor digitorum longus muscles were isolated and digested in 0.2% collagenase for 90 minutes at 37°C, as described [29]. Primary myoblasts were obtained from all hind limb muscles, according to the procedure of Musaro and Barberi [30]. C2C12 cells were obtained from the American Type Culture Collection (Rockville, MD). For antibody treatment, C2C12 cells were preincubated for 1 hour with 2.5 μg/ml of control IgG (rat IgG) or blocking antibody for CD44 (clone KM81; Abcam, Cambridge, MA) with or without BM-MSC-derived condition media. Recombinant mouse tumor necrosis factor-alpha (TNF-α)-stimulated gene/protein-6 (TSG-6) (0.5 mg/ml) was applied to stimulate the C2C12 cells for 48 hours.

Colony-Forming Unit Assay

Lin^- BMCs were collected to exclude all hematopoietic lineage cells from total BMCs by the MACS system (Miltenyi Biotec, Bergisch Gladbach, Germany). Isolated Lin^- BMCs were then seeded in a six-well plate. The adherent cells were stained as described [31]. The numbers of colonies containing more than 50 cells were counted under a light microscope.

In Vivo Migration Assay

Silicon tubes containing either PBS or SDF-1α (100 ng/ml; Peprotech, Rocky Hill, NJ) were implanted under the skin of mdx mice. After 2 days, the tubes were collected and cultured for 2 days and analyzed by immunocytochemistry.

Muscle Injury and Treatment

To induce muscle injury, a cardiotoxin (CTX; *Naja mossambica* venom; Sigma, St. Louis, MO) was used [32]. For cell treatment, freshly isolated BMCs (1×10^5) were injected directly into both the superior and inferior regions of CTX-damaged WT or mdx muscles. The day after treatment, 10 μg of CD44 antibody (clone KM81, Abcam) and 5 μg of TSG-6 antibody (clone MAB2104, R&D Systems, Minneapolis, MN) were administered to the muscles. As a control, the same amounts of rat or mouse IgG (R&D Systems) were used. Recombinant mouse TSG-6 (2 μg in 10 μl of PBS; R&D Systems) was administered to the muscles. The same volume of PBS was injected into the muscle as a control.

Histology and Immunostaining

Hematoxylin and eosin (H&E) staining was performed as described [32]. For collagen staining, a picrosirius red staining kit was used (Polysciences, Warrington, PA). The average cross-sectional area (CSA) of muscle fibers was measured using NIH ImageJ software. Only regenerating muscle fibers with central nuclei (100–300 fibers per muscle) were measured. The antibodies used for immunostaining are listed in Supporting Information Table S1. For the nuclear staining, prolong gold antifade reagent containing DAPI (Life Technologies, Carlsbad, CA) was used. The MyoD-, Pax7-, and embryonic myosin heavy chain (eMyHC)-positive cells and the area in three regions of cross-section per mouse were determined by NIH ImageJ software.

Evans Blue Dye Uptake

First, 10 mg/ml of Evans blue dye (EBD) stock solution was prepared in PBS. A single dose (50 mg/g of b.wt.) was administered to the mouse by intraperitoneal injection. The mice were sacrificed 20 hours later, and the muscles were dissected. The EBD^+ cells per muscle were counted in five regions using ×20 magnification sections.

Fluorescence-Activated Cell Sorting Analysis and Sorting of Bone Marrow Cells

Isolated BMCs containing 2×10^6 cells were suspended in 200 μl of staining buffer (2% FBS in PBS), followed by an incubation with purified rat anti-mouse CD16/CD32 (Mouse BD Fc Block, BD Pharmingen, San Diego, CA) for 10 minutes at 4°C. The fluorescence-conjugated antibodies were incubated for 30 minutes at 4°C. The antibodies used in the flow cytometry analysis are listed in Supporting Information Table S1. Fluorescence was measured by the FACSCanto II (BD Biosciences). Gates were defined based on the isotype control staining. The fluorescence-activated cell sorting data were analyzed using FlowJo software ver. 6.3.3 (Tree Star, Ashland, OR).

Muscle Digestion for the Flow Cytometry Analysis

The harvested muscles (soleus, tibialis anterior [TA], gastrocnemius, and plantaris) were minced into small pieces and digested using 0.2% collagenase A (Roche, Mannheim, Germany) for 40 minutes at 37°C with frequent triturating by pipette. The digested muscles were centrifuged at 1,200 rpm for 5 minutes and then further incubated in 0.2% collagenase/dispase (Roche) for 1 hour at 37°C. Following digestion, the cells were filtered using a sequence of 70-μm and 40-μm nylon mesh strainers, followed by centrifugation at 1,500 rpm for 10 minutes. The pellets were then suspended in the staining buffer and stained with specific antibodies, and the BMC populations in damaged muscles were analyzed and isolated by the BD FACSCanto II and BD FACSAria II, respectively.

Western Blot Analysis

Western blot analyses were performed as described [32]. The antibodies used in the Western blot analysis are listed in Supporting Information Table S1. All bands were visualized by Chemi-Lumi One (Nacalai Tesque, Kyoto, Japan) with ImageQuant LAS 4000mini software (GE Healthcare, Buckinghamshire, U.K.). The band density was analyzed using NIH ImageJ software.

RNA Extraction and Real-Time Polymerase Chain Reaction

Total RNA was extracted from muscle and BMCs using ISOGEN (Nippon Gene, Toyama, Japan) according to the manufacturer's instructions. cDNA was synthesized from an equal quantity of total RNA (2 μg for muscle and 500 ng for sorted BMCs) by reverse transcription using the High Capacity RNA-to-cDNA kit (Applied Biosystems, Foster City, CA). A real-time polymerase chain reaction (PCR) was performed with SYBR PremixEX Taq (Takara Bio, Shiga, Japan) using oligonucleotide primers. The sequences of oligonucleotide primers used for the real-time PCR are listed in Supporting Information Table S2. The quantitative data were obtained in triplicate within a single experiment on a 384-well plate based on the standard curve method using CFX manager software (BioRad, Hercules, CA). All data were normalized to GAPDH levels as an internal control.

RNA Sequencing

RNA was extracted from sorted $Lin^-/ckit^-/CD106^+/CD44^+$ and $Lin^-/ckit^-/CD106^+/CD44^-$ BMCs using ISOGEN (Nippon

Gene) according to the manufacturer's instructions. Strand-specific sequencing libraries from two biological replicate RNA samples were prepared according to the Life Technologies protocol, as described [33]. Briefly, digested poly-A-tailed RNA was ligated to the SOLiD Adaptor Mix and then reverse-transcribed using the SOLiD Total RNA-Seq Kit (Life Technologies). Size-selected first-strand cDNA was amplified by SOLiD 5′ PCR primers and barcoded SOLiD 3′ PCR primers (Life Technologies). RNA-seq libraries were sequenced with the 5500xl Genetic Analyzer (Life Technologies). The resulting reads were mapped using Lifescope (Life Technologies) and analyzed using Cufflinks and CummeRbund [34, 35]. The enrichment of gene ontology was calculated by gene ontology tool Database for Annotation, Visualization, and Integrated Discovery [36, 37].

Statistical Analyses

The values are expressed as the mean ± SEM. Statistical analyses were performed with Student's t test using the SPSS ver. 10.0 (Japan, Inc., Tokyo). For all statistical tests, significance was accepted at $p < .05$.

Accession Numbers

The accession number of RNA seq data is DRA002440.

Results

WT and mdx Mouse Bone Marrow Transplantations Showed Different Effects on mdx Muscle Pathology

We first examined whether the transplantation of WT BMCs in mdx mice would ameliorate muscle pathology by restoring dystrophin expression. To address this question, we transplanted BMCs derived from either 10-week-old WT mice (or 10-week-old GFP mice) or mdx mice into lethally irradiated 3–4-week-old mdx mice to generate BMT mice (Fig. 1A; Mdx-wt vs. Mdx-mdx, Supporting Information Fig. S4A; Mdx-GFP). To clarify the influence of BMT itself on muscle pathology, we used age-matched non-BMT mdx mice as controls. The body weights and muscle wet weights were not significantly different between the groups during the experimental period (Supporting Information Fig. S1A, S1B).

We did not detect any BM-derived (GFP^+) myofibers in the soleus muscles of the Mdx-GFP mice (Supporting Information Fig. S4A, S4B) or in the cardiotoxin (CTX)-damaged TA muscles (Supporting Information Fig. S4C, S4D), indicating that BM-derived myofibers are negligible, if any, in the mdx mouse after BMT. However, we found significantly increased collagen deposition, which is a marker of fibrosis, in soleus muscles of the Mdx-mdx mice compared with those of Mdx-wt and Mdx (age-matched non-BMT) mice 7 weeks after BMT (Fig. 1B). The aged-matched, non-BMT mdx mice showed less collagen staining compared with the Mdx-wt mice (Fig. 1B), suggesting certain adverse effects of the lethal-dose irradiation in the BMT procedure on muscle pathology in mdx mice.

To obtain quantitative data for fibrosis [27], we measured the levels of fibronectin and MMP13 in soleus muscles 7 weeks after BMT and found that these fibrosis markers were also significantly higher in the Mdx-mdx mice than in Mdx-wt and Mdx mice (Fig. 1C, 1D; Supporting Information Fig. S1C). MMP13 expression is regulated by TNF-α. TNF-α expression tended to be higher in Mdx-mdx mice than in Mdx-wt and Mdx mice (Supporting Information Fig. S1D), suggesting that TNF-α and MMP13 participate, at least in part, in fibrotic deposition.

In contrast, the expression of TNF-α-stimulated gene/protein-6 (TSG-6), which is an anti-inflammatory mediator, was slightly higher in Mdx-wt mice compared with Mdx-mdx mice (Supporting Information Fig. S1E). EBD staining of soleus muscles 7 weeks after BMT showed greatly enhanced necrotic tissue damage in Mdx-mdx mice compared with Mdx-wt and Mdx mice (Fig. 1E, 1F), suggesting increased necrosis by excess inflammation or decreased overall repair mechanisms in Mdx-mdx mice.

We next analyzed the muscle strength and endurance of those BMT mice from 4 to 7 weeks after BMT using grip strength (Fig. 1G) and two different hang wire tests (Supporting Information Fig. S1F, S1G) [28]. Consistent with the deterioration of muscle pathology observed in the Mdx-mdx mice, the muscle functions in Mdx-mdx mice were significantly lower than those of Mdx-wt and Mdx mice (Fig. 1G; Supporting Information Fig. S1F, S1G). These results suggest that mdx-related alterations in BM have significant adverse effects on the progression of muscular degeneration, whereas normal BMT in mdx mice can rescue this mechanism without dystrophin supplementation.

Chronic Muscle Injury in mdx Mice Induced a Reduction of MSC Populations in BM

In the mdx mouse, massive muscle degeneration starts at approximately 3–4 weeks of age, and the degeneration/regeneration cycle continues throughout the lifespan, although muscle degeneration is milder after 12 weeks of age [38]. We thus examined whether the numbers of BM-MSCs in 10-week-old mdx mice were altered as a result of the systemic effect of the chronic muscle degeneration/regeneration cycle. We used a CFU-F assay to determine the total numbers of MSCs in the BM of 10-week-old mdx mice.

Strikingly, the number of BM CFU-Fs in 10-week-old mdx mice was significantly decreased compared with those in the WT mice (Fig. 2A). BM-MSCs have been shown to be highly heterogeneous. We thus investigated the subpopulations of BM-MSCs in 10-week-old mdx mice by conducting flow cytometry analysis. Both CD106 and CD44 have been reported as being expressed in cultured BM mesenchymal "stem" cells [6]. However, a recent report suggests that freshly isolated BM mesenchymal stem cells do not express CD44, and therefore, the expression of CD44 on MSCs in BM remains controversial [18].

Interestingly, in this study, both the $Lin^-/ckit^-/CD106^+/CD44^+$ and $Lin^-/ckit^-/CD106^+/CD44^-$ subpopulations in BM were greatly reduced in 10-week-old mdx mice (Fig. 2B, 2C), but the percentage of the $Lin^+/ckit^-$ population in BM, which includes mature hematopoietic lineage cells [24], was not significantly different between the 10-week-old mdx and WT mice (Supporting Information Fig. S5A). These differences between WT and mdx mice were not observed at 3 weeks of age, before or immediately after the onset of DMD (Supporting Information Fig. S5B–S5F). The results thus suggest that the reduction of these BM subpopulations depends on DMD progression.

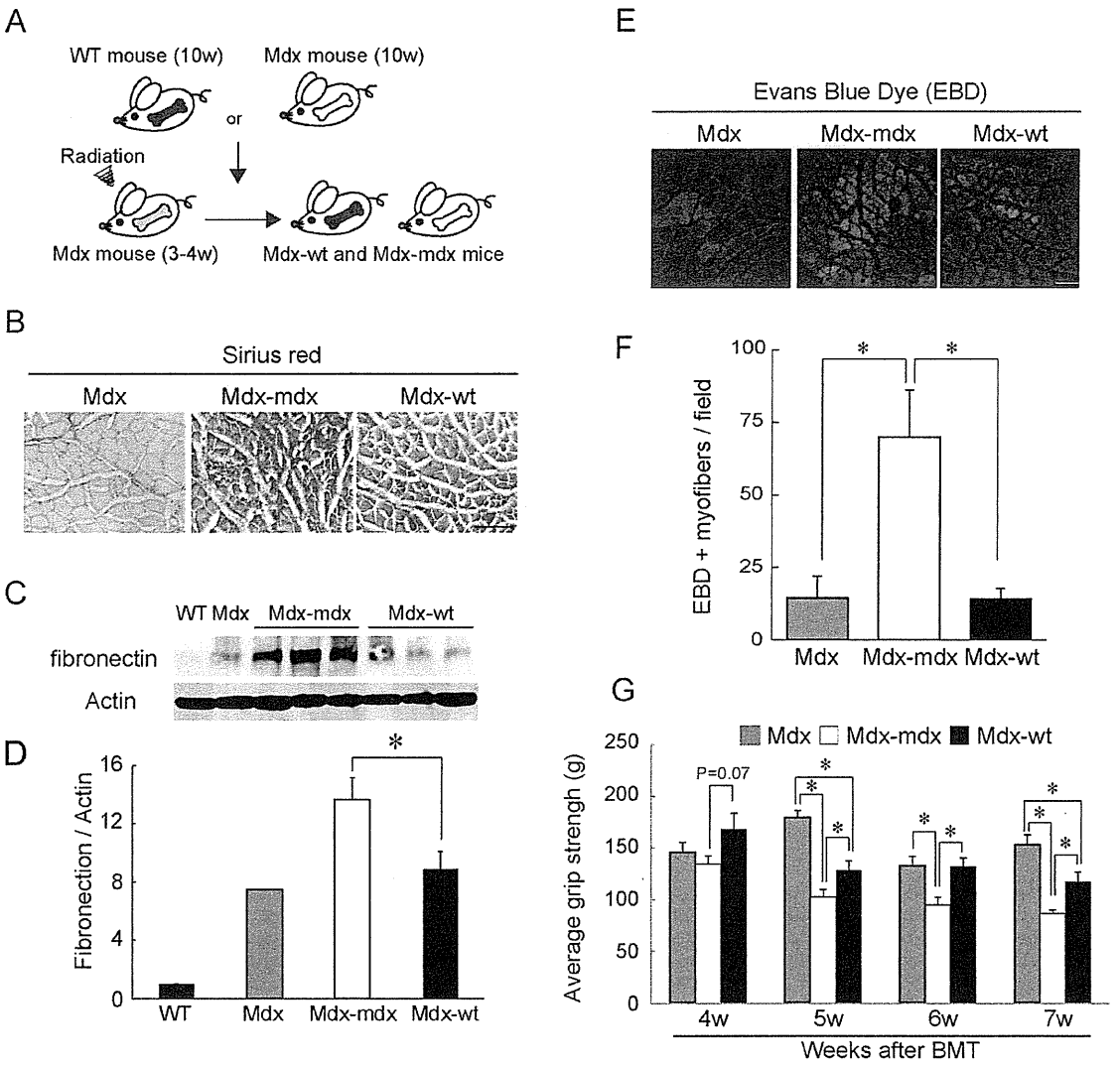

Figure 1. Effects of 10-week-old WT or mdx bone marrow cell (BMC) transplantation on Duchenne muscular dystrophy muscle pathology. **(A):** Schematic illustration of the experimental models. Either 10-week-old WT mouse BMCs or mdx mouse BMCs were transplanted into 3–4-week-old mdx mice after lethal-dose irradiation (Mdx-wt and Mdx-mdx). **(B):** Representative soleus muscle sections of Mdx (age-matched non-BMT control), Mdx-wt, and Mdx-mdx mice stained by picrosirius red 7 weeks after BMT. Scale bar = 200 μm. **(C):** Western blot analyses of fibronectin and Pan-actin (loading control) of soleus muscle 7 weeks after BMT. **(D):** Quantified band densities of fibronectin/actin. The values are the mean ± SEM; *, $p < .05$. **(E):** Representative soleus muscle sections of Mdx (age-matched non-BMT control), Mdx-wt, and Mdx-mdx mice visualized by Evans blue dye (EBD) 7 weeks after BMT. Scale bar = 100 μm. **(F):** The number of EBD^+ fibers was quantified. The values are the mean ± SEM ($n = 4$); *, $p < .05$. **(G):** Measurement of grip strength in Mdx (age-matched non-BMT control), Mdx-wt, and Mdx-mdx mice from 4 to 7 weeks after BMT. The values are the mean ± SEM ($n = 7$–8/group); *, $p < .05$. Abbreviation: BMT, bone marrow transplantation.

To exclude the possibility that these reductions of specific BM subpopulations were simply the result of different degrees of cellularity in dystrophin-deficient BMCs, we established three types of BMT models (Fig. 2D). BMCs from 3-week-old WT mice (donor) were transplanted into either 3-week-old WT (WT-wt) or mdx mice (Mdx-wt) after a lethal dose of irradiation, which replaces the host BMCs with donor BMCs (Supporting Information Fig. S2A, S2B). As another control, BMCs from a 3-week-old mdx mouse (donor), which had BM subpopulations and CFU-F numbers identical to those of WT mice (Supporting Information Fig. S5B–S5F), were transplanted into 3-week-old WT mice (WT-mdx). Both the $Lin^-/ckit^-/CD106^+/CD44^+$ and $Lin^-/ckit^-/CD106^+/CD44^-$ subpopulations in the Mdx-wt mice were significantly lower than those in the WT-wt and WT-mdx mice (Fig. 2E, 2F). These results suggest that both the $Lin^-/ckit^-/CD106^+/CD44^+$ and $Lin^-/ckit^-/CD106^+/CD44^-$ BM subpopulations were gradually reduced by chronic exposure to a muscle injury environment after the onset of muscular dystrophy.

Whole-Transcriptome Analysis of the Reduced MSC Populations in mdx Mice

We further investigated the precise properties of endogenous $Lin^-/ckit^-/CD106^+/CD44^+$ and $Lin^-/ckit^-/CD106^+/CD44^-$ BM populations. PDGFRα has been reported to be expressed in mesenchymal lineage cells [39, 40]. We therefore examined

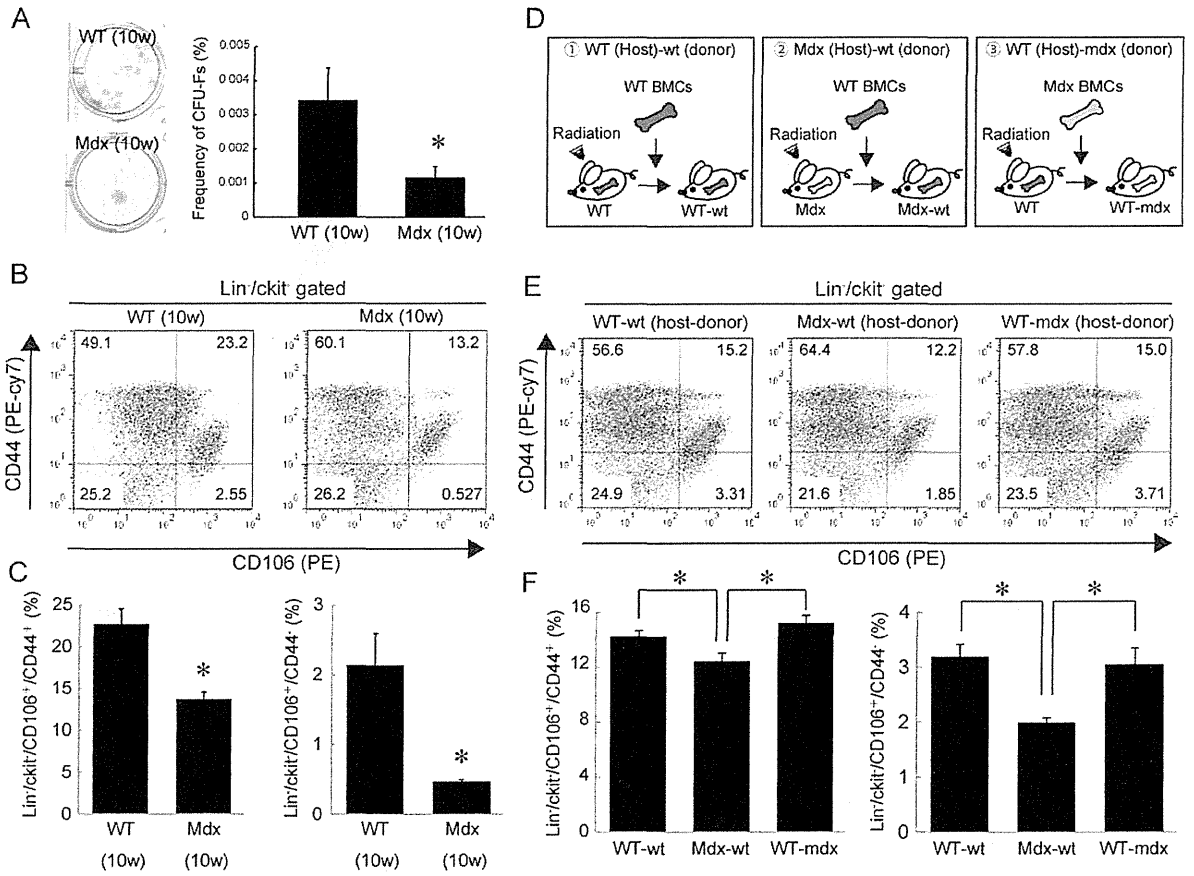

Figure 2. Reduction of mesenchymal stromal cell populations in bone marrow (BM) by chronic muscle injury in mdx mice. **(A):** The numbers of Lin^- cells in the BM of 10-week-old WT and Mdx mice were analyzed in a CFU-F assay. The frequency of CFU-Fs is expressed as the mean ± SEM ($n = 6$/group); *, $p < .05$. **(B):** Representative fluorescence-activated cell sorting (FACS) profiles of BMCs in 10-week-old WT and Mdx mice BM, stained with Lin, ckit, CD106, and CD44. FACS charts gated within $Lin^-/ckit^-$ cells are shown. **(C):** The percentages of $CD106^+/CD44^+$ and $CD106^+/CD44^-$ cells gated within $Lin^-/ckit^-$ cells were quantified. The values are the mean ± SEM ($n = 6$/group); *, $p < .05$. **(D):** Scheme of the bone marrow transplantation (BMT) models, which indicates the following: (1) 3-week-old WT BMCs were transplanted into preirradiated 3-week-old WT mice (WT-wt); (2) 3-week-old WT BMCs were transplanted into preirradiated 3-week-old Mdx mice (Mdx-wt); and (3) 3-week-old Mdx BMCs were transplanted into preirradiated 3-week-old WT mice (WT-mdx). **(E):** Representative FACS profiles of BMCs 7 weeks after BMT, stained with Lin, ckit, CD106, and CD44. FACS plot gated within $Lin^-/ckit^-$ cells is shown. **(F):** The percentages of $CD106^+/CD44^+$ and $CD106^+/CD44^-$ cells gated within $Lin^-/ckit^-$ cells were quantified. The values are the mean ± SEM ($n = 4$/group); *, $p < .05$. Abbreviation: BMC, bone marrow cell.

PDGFRα expression in these BM populations using PDGFRα-H2B GFP mice (see Materials and Methods). $Lin^-/ckit^-/CD106^+/CD44^+$ and $Lin^-/ckit^-/CD106^+/CD44^-$ BM populations comprised 19.9% and 71.9% of the PDGFRα-expressing cells, respectively (Fig. 3A, 3B), suggesting that both of these BM populations contain $PDGFR\alpha^+$ mesenchymal lineage cells.

Next, we conducted a whole-transcriptome analysis by RNA sequencing (RNA seq) analyses to further investigate the molecular properties of these populations. We sorted $Lin^-/ckit^-/CD106^+/CD44^+$ and $Lin^-/ckit^-/CD106^+/CD44^-$ BMCs. The transcript of CD106 mRNA was enriched in the $Lin^-/ckit^-/CD106^+/CD44^+$/ and $Lin^-/ckit^-/CD106^+/CD44^-$ populations, but was not detected in any other populations (Fig. 3C), indicating a successful enrichment of these two populations. Our comparison of the whole-genome transcriptome revealed the enrichment of different functional clusters in each population (Fig. 3D, 3E). The $Lin^-/ckit^-/CD106^+/CD44^+$ population showed significantly higher expression levels of genes, including DNA replication- and cell cycle-related genes (Fig. 3D), such as Myc and Mcm2 (Fig. 3F). In contrast, these genes were not expressed in the $Lin^-/ckit^-/CD106^+/CD44^-$ population. The $Lin^-/ckit^-/CD106^+/CD44^-$ population showed significantly higher expression levels of genes, including cell adhesion- and extracellular matrix receptor interaction-related genes (Fig. 3E). CXCL12 (SDF-1α), Col1A, and FGFR1, which have been reported to be expressed in HSC niche cells [10, 14, 41] (Fig. 3G; Supporting Information Fig. S6).

One of the features associated with stem cell populations is cell-cycle quiescence under physiological conditions. Therefore, to further investigate the differences in the expression of cell cycle-related genes between the two cell populations observed in the RNA seq analysis, we analyzed the expression of the nuclear proliferation marker Ki67 in a flow cytometry analysis. We found that approximately 50% of the $Lin^-/CD106^+/CD44^+$ population was $Ki67^+$, whereas only 10% of the $Lin^-/CD106^+/CD44^-$ population was $Ki67^+$

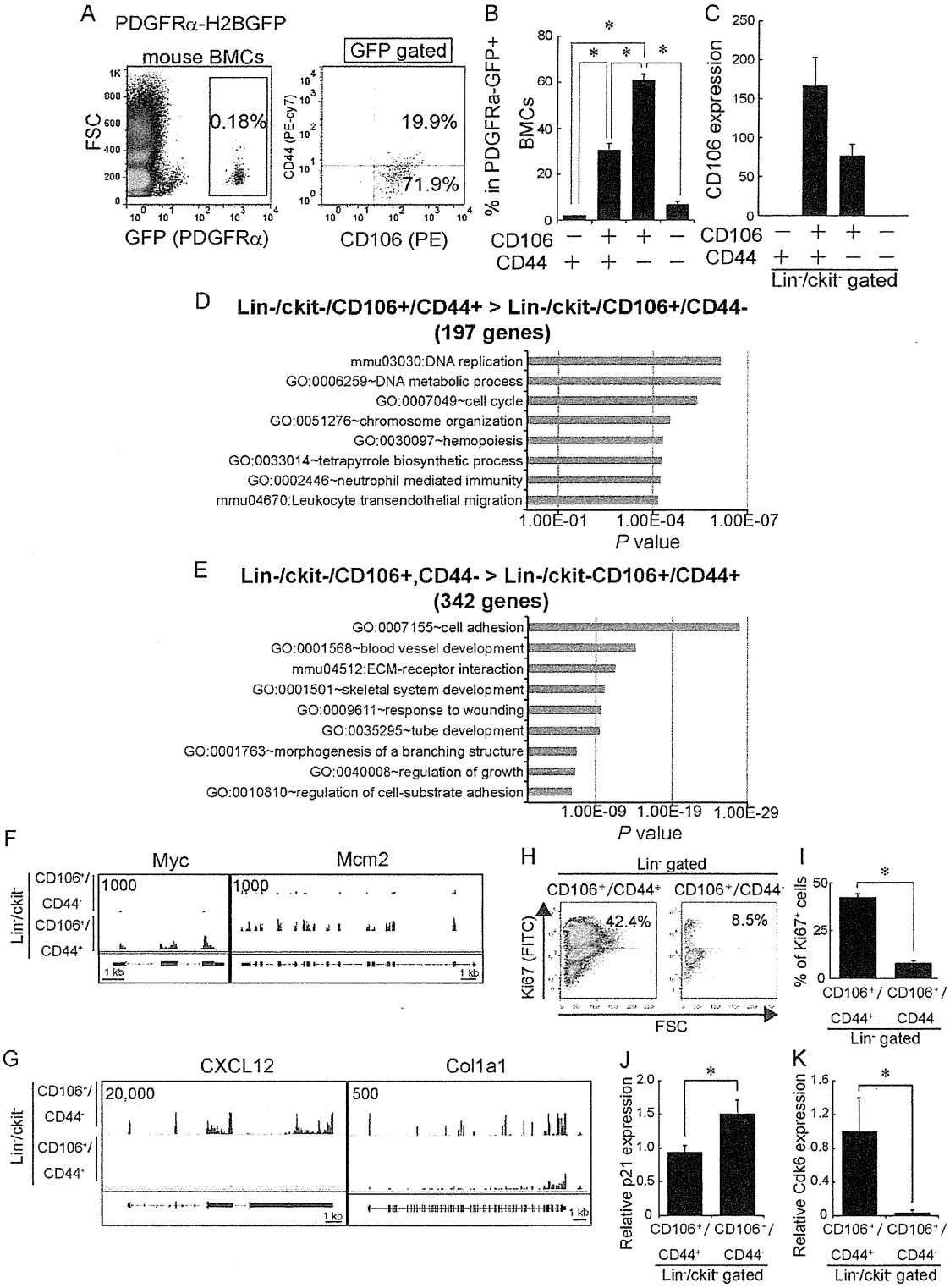

Figure 3. Prospective characterization of freshly isolated mesenchymal stromal cell populations in bone marrow. **(A):** Representative fluorescence-activated cell sorting (FACS) profiles of total BMCs in PDGFRα-H2BGFP knockin mouse. The percentage of PDGFRα-H2BGFP$^+$ cells in total BMCs is shown (left). CD106 and CD44 expression profiles in PDGFRα-GFP$^+$ cells (right). **(B):** The percentages of CD106$^+$/CD44$^+$ and CD106$^+$/CD44$^-$ cells in PDGFRα-GFP$^+$ cells were quantified. The values are the mean ± SEM ($n = 3$/group); *, $p < .05$. **(C):** CD106 mRNA expressions in sorted BMCs. The values are the mean ± SEM. The data are for three independent sorting experiments. **(D, E):** Gene ontology (GO) analysis of RNA seq data from sorted Lin$^-$/ckit$^-$/CD106$^+$/CD44$^+$ and Lin$^-$/ckit$^-$/CD106$^+$/CD44$^-$ BMCs. Genes that are significantly upregulated in Lin$^-$/ckit$^-$/CD106$^+$/CD44$^+$ BMCs (197 genes) or Lin$^-$/ckit$^-$/CD106$^+$/CD44$^+$ cells (342 genes) were categorized by GO annotations. **(F):** RNA-seq results showing the expression of cell cycle-associated genes (Myc and Mcms) in sorted Lin$^-$/ckit$^-$/CD106$^+$/CD44$^+$ and Lin$^-$/ckit$^-$/CD106$^+$/CD44$^-$ BMCs. **(G):** RNA-seq results showing the expressions of CXCL12 (SDF-1α) and Col1a1 in sorted Lin$^-$/ckit$^-$/CD106$^+$/CD44$^+$ and Lin$^-$/ckit$^-$/CD106$^+$/CD44$^-$ BMCs. The RNA-seq data were obtained from two biological replicates. **(H):** Representative FACS profiles of Ki67 expression on Lin$^-$/CD106$^+$/CD44$^+$ and Lin$^-$/CD106$^+$/CD44$^-$ BMCs. **(I):** The percentages of Ki67$^+$ cells on each population were quantified. The values are the mean ± SEM ($n = 3$); *, $p < .05$. **(J, K):** The expressions of cdk6 (J) and p21 (K). The data are for three independent sorting experiments. The values are the mean ± SEM; *, $p < .05$. Abbreviations: BMC, bone marrow cell; FSC, forward scatter; GFP, green fluorescent protein.

(Fig. 3H, 3I). Real-time PCR also revealed that p21, a cell cycle inhibitor gene, showed reduced expression in the $Lin^-/ckit^-/CD106^+/CD44^+$ population than in the $Lin^-/ckit^-/CD106^+/CD44^-$ population (Fig. 3J). In contrast, cyclin-dependent kinase 6 (cdk6) showed higher expression in the $Lin^-/ckit^-/CD106^+/CD44^+$ population than in the $Lin^-/ckit^-/CD106^+/CD44^-$ population (Fig. 3K). Together, these data suggest that $Lin^-/ckit^-/CD106^+/CD44^+$ and $Lin^-/ckit^-/CD106^+/CD44^-$ BM populations, which were decreased in 10-week-old mdx mice, were a proliferative and a slow-dividing mesenchymal lineage, respectively.

Endogenous Migration of BM-Derived MSC Population in Injured Muscles

We then investigated the recruitment of BM-derived mesenchymal populations into damaged muscles. GFP BMCs were transplanted in 3–4-week-old mdx mice (Mdx-GFP), and we analyzed the characteristics of the BM-derived cells recruited to the damaged muscles 4 weeks after BMT by flow cytometry. We found that the Lin^-/GFP^+ cells, which include BM-derived MSC populations (Supporting Information Fig. S7A, S7B), were substantially recruited into the damaged muscle of the mdx mice compared with WT muscles (red squares in Fig. 4A, 4B). Importantly, most of the Lin^-/GFP^+ cells in the damaged muscles expressed both CD106 and CD44 on their surface (red squares in Fig. 4C; Supporting Information Fig. S7C), suggesting that BM-derived $Lin^-/CD106^+/CD44^+$ cells predominantly accumulated into damaged muscle in mdx mice compared with other Lin^-/GFP^+ populations.

These results led us to examine the possible recruitment mechanism of this population. We found that CXCR4 was highly expressed in freshly isolated $Lin^-/ckit^-/CD106^+/CD44^+$ BMCs by the RNA seq (Fig. 4E) and flow cytometry analyses (Supporting Information Fig. S7D). CXCR4 is a receptor for SDF-1α and has been found to be involved in the migration of stem/progenitor cells in various tissues. To elucidate whether the SDF-1α/CXCR4 axis plays a role in recruiting $Lin^-/ckit^-/CD106^+/CD44^+$ BMCs into damaged muscles, we first compared CXCR4 expression in the $Lin^-/ckit^-/CD106^+/CD44^+$ BMCs of WT and mdx mice. We found that CXCR4 expression was slightly but not significantly elevated in the $Lin^-/ckit^-/CD106^+/CD44^+$ BM populations of mdx mice compared with those of the WT mice (Supporting Information Fig. S7E), suggesting that elevated CXCR4 levels are not responsible for the specific migration of $Lin^-/ckit^-/CD106^+/CD44^+$ BMCs into damaged muscles.

Next, we assessed SDF-1α expression in mdx soleus muscles. SDF-1α was specifically detected in mdx muscles but not WT muscles, and $CD68^+$ cells primarily colocalized with SDF-1α signals (Supporting Information Fig. S7F). We also detected significant increases in $Lin^-/ckit^-/CD106^+/CD44^+/CXCR4^+$ cells in the peripheral blood of mdx mice (Fig. 4F). In addition, we implanted silicon tubes containing recombinant SDF-1α under the skin of mdx mice. Two days later, we collected the tubes and counted the numbers and percentages of adherent $CD106^+/CD44^+$ tube-trapped cells. As shown in Supporting Information Figure S7G, S7H, significantly more $CD106^+/CD44^+$ cells migrated into the SDF-1α-containing tubes compared with the tubes containing PBS. These results suggest that the migration of $Lin^-/ckit^-/CD106^+/CD44^+$ BMCs into damaged muscles although the circulation may be partially explained, if not exclusively so, by the CXCR4-SDF-1α pathway.

Function of the BM-Derived MSC Population in Damaged Muscles

Because the TSG-6-mediated immunosuppressive function of cultured expanded MSCs has been documented [42], we next investigated the expression of TSG-6 in the BM-derived $Lin^-/CD106^+/CD44^+$ population in the damaged muscles of Mdx-GFP mice. We found that BM-derived $(GFP^+)/Lin^-/CD106^+/CD44^+$ cells significantly and preferentially expressed TSG-6 in damaged muscles compared with other BM-derived populations (Fig. 5A). However, interleukin-10, which has also been reported to be expressed in BM-MSCs, was not detected (data not shown). It is well known that TSG-6 suppresses inflammation by interacting with CD44 on inflammatory cells, but we also observed the expression of CD44 on the C2C12 myoblasts and primary satellite cells (Fig. 5B; Supporting Information Fig. S8A, S8B). Recombinant TSG-6 (rTSG-6) significantly augmented the proliferation of C2C12 myoblasts (Fig. 5C), suggesting that TSG-6 from BM-MSCs also activated myoblasts.

A previous study suggested that damage signals enhanced TSG-6 expression in BM-MSCs [3], and thus, we investigated whether the treatment of primary BM-MSCs with mdx mouse serum (which contains damage signals) would enhance TSG-6 expression (Fig. 5D). As shown in Figure 5E, elevated TSG-6 expression in mdx serum-treated BM-MSCs was observed, suggesting that the recruited BM-MSC population exposed to damage signals in mdx mice likely elevates TSG-6 expression to suppress inflammation and to activate myoblasts in the damaged muscles.

We also cocultured C2C12 myoblasts with conditioned medium (CM) from BM-MSCs treated with mdx mouse serum for 48 hours (Fig. 5D). We observed a significant proliferation of C2C12 myoblasts following CM treatment (Fig. 5F). However, the CM-mediated C2C12 proliferation was moderately but significantly blocked in the presence of a CD44-neutralizing antibody (Fig. 5F). These data suggest that the TSG-6 secreted from activated BM-MSCs stimulates myoblast activation.

BM-Derived $Lin^-/ckit^-/CD106^+/CD44^+$ Cells Accelerated Muscle Regeneration

Lastly, we examined whether the $Lin^-/ckit^-/CD106^+/CD44^+$ BMCs, the main source of TSG-6 in damaged muscles, could support muscle regeneration. To minimize the effect of the endogenous BM-MSCs population during muscle regeneration, we generated mice with reduced MSCs in BM ($ckit^+$ BMT) by transplanting a sorted $Lin^-/ckit^+$ population (including HSCs but not MSCs) after lethal-dose irradiation (Supporting Information Fig. S3A). As shown in Supporting Information Figure S3B, S3C, the percentage of the $Lin^-/ckit^-$ population in the BM, which includes an MSC population, was significantly less in the $ckit^+$ BMT mice compared with the total BMT mice after 6 weeks of reconstitution. Furthermore, fewer donor BM-derived fibroblastic cells were observed in the $ckit^+$ BMT mice compared with the total BMT mice (Supporting Information Fig. S3D–S3F). These data indicate that $ckit^+$ BMT mice have few endogenous MSCs in their BM.

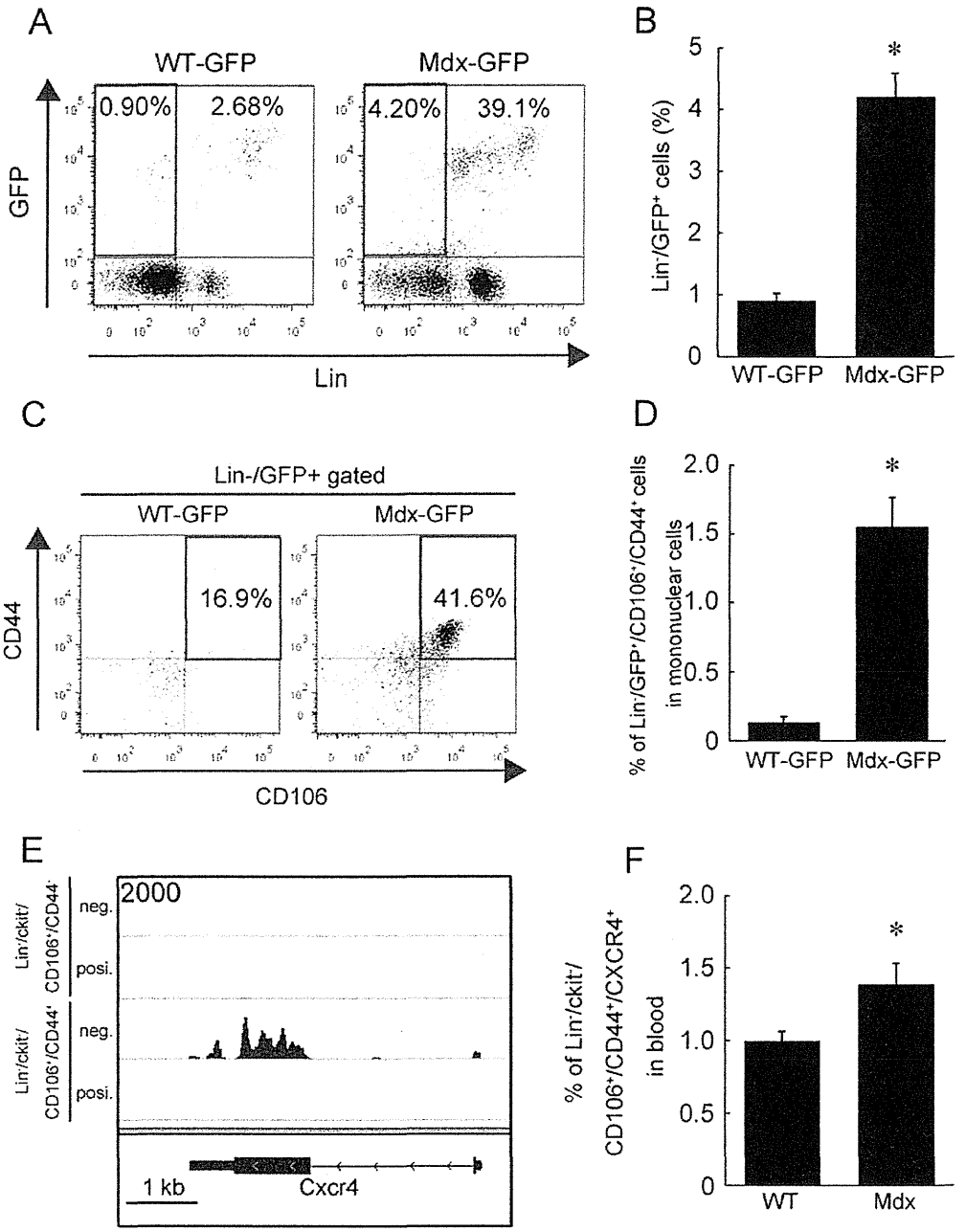

Figure 4. Identification of bone marrow (BM)-mesenchymal stromal cell populations in mdx muscles. **(A):** Flow cytometry analysis in muscles of WT-GFP (left) and Mdx-GFP (right) bone marrow transplantation (BMT) mice performed 4 weeks after BMT. The red squares indicate Lin^-/GFP^+ cells (BM-derived nonhematopoietic cells). **(B):** The percentages of Lin^-/GFP^+ cells were quantified. The values are the mean ± SEM ($n = 4$); *, $p < .05$. **(C):** CD106 and CD44 expression in Lin^-/GFP^+ cells in the muscles of Mdx-GFP BMT mice. Most of the Lin^-/GFP^+ cells were positive for both CD106 and CD44 (red squares). The percentages of $CD106^+/CD44^+$ cells in Lin^-/GFP^+ cells in mdx muscles are shown with red squares. **(D):** The percentages of $Lin^-/GFP^+/CD106^+/CD44^+$ cells in mdx muscles were evaluated. The values are the mean ± SEM ($n = 4$); *, $p < .05$. **(E):** CXCR4 expression from the RNA seq analysis of sorted $Lin^-/ckit^-/CD106^+/CD44^+$ and $Lin^-/ckit^-/CD106^+/CD44^-$ bone marrow cells. **(F):** The percentages of $Lin^-/ckit^-/CD106^+/CD44^+/CXCR4^+$ cells in the peripheral blood of WT and mdx mice were quantified by flow cytometry. The values are the mean ± SEM ($n = 6$–8); *, $p < .05$. Abbreviation: GFP, green fluorescent protein.

Using the $ckit^+$ BMT model, we investigated whether an intramuscular injection of $Lin^-/ckit^-/CD106^+/CD44^+$ BMCs would enhance muscle regeneration in CTX-induced damaged muscles of WT-$ckit^+$ BMT mice (Supporting Information Fig. S9). At 14 days post-treatment, H&E staining showed well-arranged myofibers with fewer mononuclear cells in damaged muscles treated with $Lin^-/ckit^-/CD106^+/CD44^+$ BMCs compared with PBS-treated or $Lin^-/ckit^-/CD106^-/CD44^+$ BMCs-treated damaged muscles, which were the second-most recruited BMCs into damaged muscles (Supporting Information Fig. S9A).

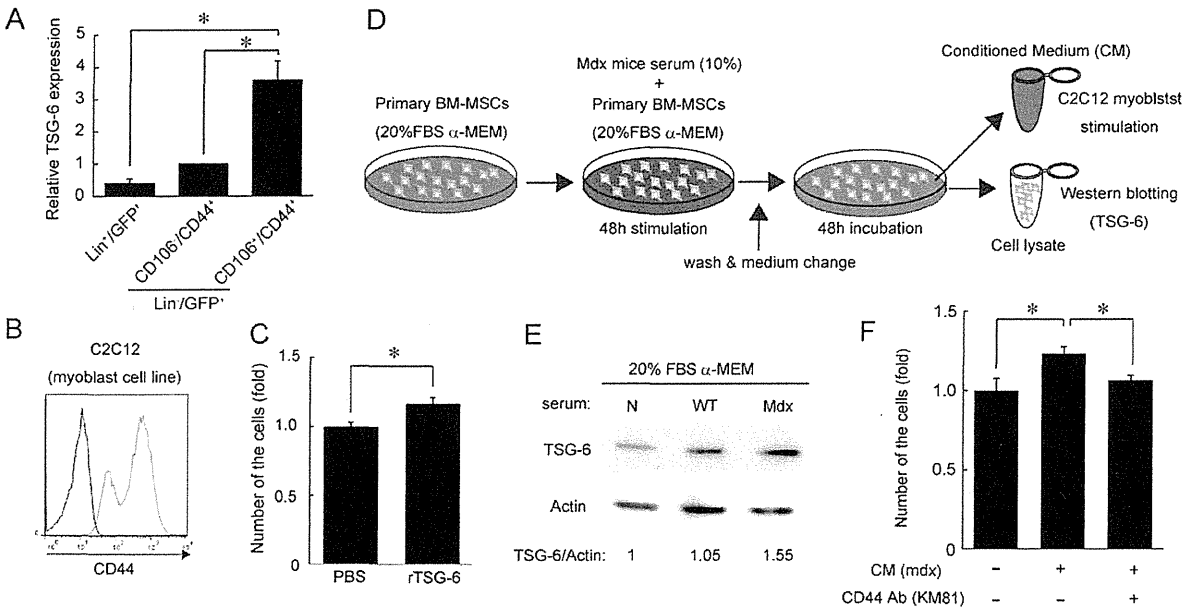

Figure 5. Effect of TSG-6 secreted from BM-MSC populations on myoblasts. **(A):** TSG-6 expression in sorted BM-derived cells from mdx muscles. The values are the mean ± SEM. The data are for three independent sorting experiments; *, $p < .05$. **(B):** Representative fluorescence-activated cell sorting profiles of CD44 expression on C2C12 myoblasts (red line). Isotype control staining is represented by the black line. **(C):** The number of C2C12 myoblasts treated with TSG-6 after 48 hours. **(D):** Strategy for the preparation of CM from primary BM-MSCs. **(E):** Western blot analyses of TSG-6 and Pan-actin (loading control) expression in primary BM-MSCs prepared as in panel (D). **(F):** The number of C2C12 myoblasts treated with CM containing either control IgG (rat IgG) or CD44-blocking antibody (KM81) for 48 hours. The values are the mean ± SEM ($n = 3$); *, $p < .05$. Abbreviations: BM-MSCs, bone marrow-mesenchymal stromal cells; CM, conditioned medium; FBS, fetal bovine serum; PBS, phosphate-buffered saline.

We quantified newly regenerating myofibers or myotubes by counting the desmin$^+$ cells with central nuclei, and the results indicated that the Lin$^-$/ckit$^-$/CD106$^+$/CD44$^+$ BMCs significantly increased the number of desmin$^+$ cells with central nuclei compared with the number in PBS-treated damaged muscles (Supporting Information Fig. S9B, S9C). We also investigated eMyHC$^+$ cell areas in damaged muscle sections. The percentage area of the eMyHC$^+$ cell area was increased by Lin$^-$/ckit$^-$/CD106$^+$/CD44$^+$ BMC treatment compared with PBS- or Lin$^-$/ckit$^-$/CD106$^-$/CD44$^+$ BMC-treated damaged muscle (Supporting Information Fig. S9D, S9E). These data suggest that Lin$^-$/ckit$^-$/CD106$^+$/CD44$^+$ BMCs accelerate muscle regeneration processes in CTX-induced muscle damage.

We next investigated whether Lin$^-$/ckit$^-$/CD106$^+$/CD44$^+$ BMC treatment supports muscle regeneration in Mdx mice. Using Mdx-ckit$^+$ BMT mice reconstituted for 6 weeks (10-week-old mice), we first assessed the effect of Lin$^-$/ckit$^-$/CD106$^+$/CD44$^+$ BMC treatment on satellite cell activation 7 days after cell injection. The injection of Lin$^-$/ckit$^-$/CD106$^+$/CD44$^+$ BMCs increased the number of activated satellite cells, as indicated by MyoD staining (Fig. 6A, 6B). We also observed slightly elevated MyoD expression after Lin$^-$/ckit$^-$/CD106$^+$/CD44$^+$ BMC treatment by Western blotting (Fig. 6C). However, the elevation of the number of MyoD$^+$ satellite cells was partially inhibited by the administration of a CD44-neutralizing antibody or a TSG-6 antibody (Fig. 6A, 6B). MyoD expression also tended to be decreased by the CD44-neutralizing antibody or TSG-6 antibody (Fig. 6C). The number of Pax7$^+$ cells and the expression level of Pax7, which is a quiescent satellite cell marker, were not significantly changed by Lin$^-$/ckit$^-$/CD106$^+$/CD44$^+$ BMC treatment (Supporting Information Fig. S10A–S10C).

We also observed that Lin$^-$/ckit$^-$/CD106$^+$/CD44$^+$ BMC treatment suppressed the infiltration of inflammatory cells and enhanced the overall muscle repair mechanisms in Mdx-ckit$^+$ BMT mice, as assessed by the average muscle fiber CSA at day 7 post-treatment (Fig. 6D, 6E). However, again, the effects of Lin$^-$/ckit$^-$/CD106$^+$/CD44$^+$ BMC treatment on muscle regeneration were partially blocked by a CD44-neutralizing antibody or a TSG-6 antibody (Fig. 6D, 6E). Of note, recombinant TSG-6 treatment also enhanced muscle regeneration with Lin$^-$/ckit$^-$/CD106$^-$/CD44$^+$ BMC treatment (Fig. 6D, 6E). These data may indicate that the BM-derived Lin$^-$/ckit$^-$/CD106$^+$/CD44$^+$ population slowed muscle disease progression by the activation of satellite cells and the suppression of inflammation to enhance the overall repair mechanisms, in part via the TSG-6/CD44-mediated pathway.

DISCUSSION

In this study, we demonstrated for the first time that injured muscular tissues in DMD mice recruit a Lin$^-$/ckit$^-$/CD106$^+$/CD44$^+$ mesenchymal population from the BM to suppress inflammatory and fibrotic reactions and activate a muscular regeneration mechanism. Such chronic injury/regeneration cycles in DMD mice were shown to eventually decrease the MSC populations in BM, resulting in a disruption of the intrinsic anti-inflammatory and regeneration-promoting activities of BM-MSCs to exacerbate muscular dystrophy (Fig. 7).

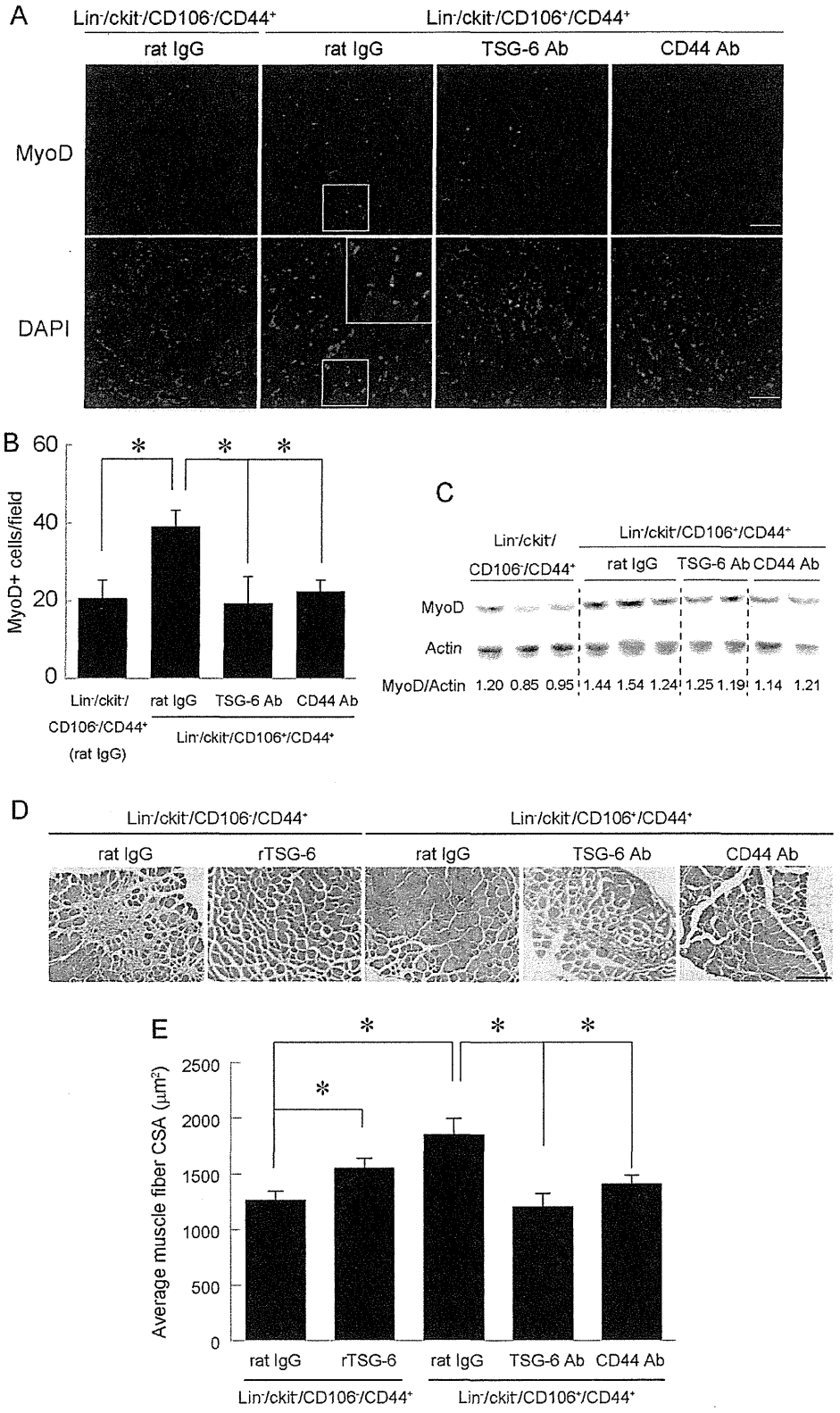

Figure 6. Effect of specific bone marrow-mesenchymal stromal cell populations on skeletal muscle regeneration. **(A):** Immunofluorescent staining for MyoD (red) on tibialis anterior (TA) muscle of Mdx-ckit$^+$ BMT mice 7 days post-treatment of Lin$^-$/ckit$^-$/CD106$^-$/CD44$^+$ or Lin$^-$/ckit$^-$/CD106$^+$/CD44$^+$ bone marrow cells (BMCs) in combination with either a CD44 antibody (KM81) or a TSG-6 antibody. Nuclei were stained with DAPI (blue). Scale bars = 50 μm. **(B):** MyoD$^+$ cells were quantified. The values are the mean ± SEM (n = 3–4/group); *, $p < .05$. **(C):** Western blot analyses of MyoD and Pan-actin (loading control) of TA muscles of Mdx-ckit$^+$ BMT mice at 7 days post-treatment of Lin$^-$/ckit$^-$/CD106$^-$/CD44$^+$ or Lin$^-$/ckit$^-$/CD106$^+$/CD44$^+$ BMCs in combination with either a CD44 antibody (KM81) or a TSG-6 antibody. Quantified band densities of MyoD normalized to actin are also shown. **(D):** H&E staining on TA muscle of Mdx-ckit$^+$ BMT mice 7 days post-treatment of Lin$^-$/ckit$^-$/CD106$^-$/CD44$^+$ or Lin$^-$/ckit$^-$/CD106$^+$/CD44$^+$ BMCs in combination with either recombinant TSG-6 or CD44 antibody (KM81) or TSG-6 antibody. Scale bar = 200 μm. **(E):** The average CSA of muscle fibers with central nuclei was quantified. The values are the mean ± SEM (n = 4–8/group); *, $p < .05$. Abbreviation: CSA, cross-sectional area.

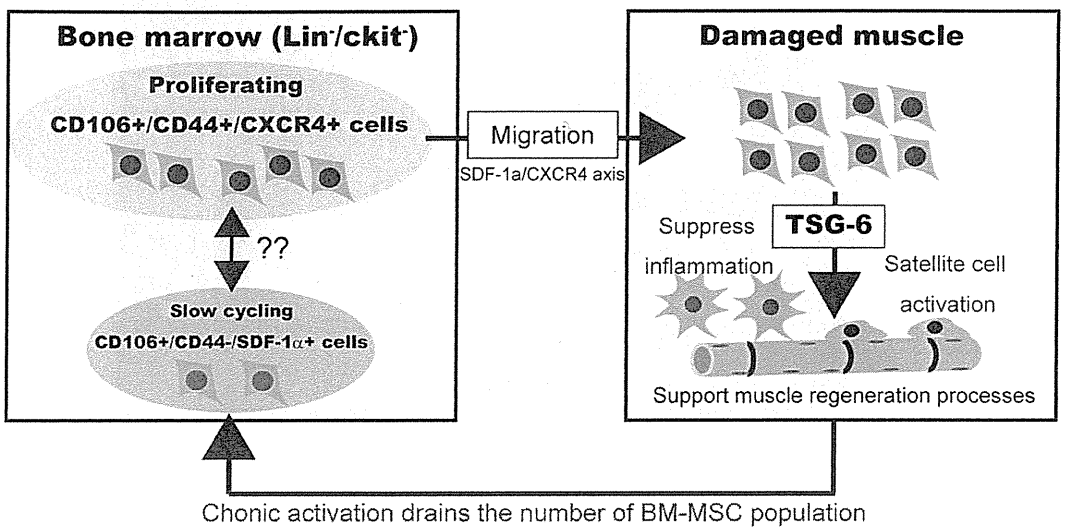

Figure 7. Schematic summary of the present findings. The $Lin^-/ckit^-/CD106^+/CD44^+$ BMC population abundantly migrates into damaged muscles to suppress inflammation and activate the muscle regeneration processes in Duchenne muscular dystrophy, in part via the TSG-6-mediated pathway. Chronic injury/regeneration cycles drain the numbers of both $Lin^-/ckit^-/CD106^+/CD44^+$ and $Lin^-/ckit^-/CD106^+/CD44^-$ populations in BM. Abbreviation: BM-MSCs, bone marrow-mesenchymal stromal cells.

Hagiwara et al. proposed that BMT did not significantly improve the muscle function of mdx mice [43] compared with non-BMT mdx mice, which is consistent with this study. For BMT, the recipient mice receive high-dose irradiation that ablates not only bone marrow cells but also other cells to worsen the regeneration ability. Therefore, in our study, we first conducted the 10-week-old mdx or WT mouse BMC transplantation into 3–4-week-old mdx mice (Mdx-wt vs. Mdx-mdx) to compare these two BMT models on mdx mouse pathology. Although muscle differentiation from BMCs was almost undetectable, we observed muscle function and pathological differences between these mice. From that point, we hypothesized and investigated whether the differences in the WT and mdx BM-MSC populations and the alteration of BM-MSC populations could be related to muscle pathological conditions in mdx mice.

Several possibilities could account for the reduction of BM-MSC populations in 10-week-old mdx mice. We previously reported that transient reduction of the $CD45^-/CD44^+/CXCR4^+$ cells in BM with appearance of this population in peripheral blood during ectopic bone formation [8]. In addition, during the inflammation phase in multiple sclerosis mice, interferon-gamma secreted from activated T cells decreased the number of CFU-Fs and $CD45^-$ cells in BM [44]. These data suggest that induction of direct or indirect stimuli in pathological conditions can mobilize MSC populations from BM to contribute to tissue regeneration at a distant location. In mdx mice, these stimuli from degenerated muscles are expected to chronically continue because the muscle pathological symptoms have progressed. Thus, the continuous requirement to contribute to muscle regeneration from BM might be responsible for the reduction in the BM-MSC population in mdx mice (Fig. 7). Previously, we reported that HMGB1 is abundantly released from necrotic epithelial cells of the mouse skin graft model and mobilizes $PDGFR^+$ cells from BM into the circulation [9]. In DMD mice, however, we did not observe HMGB1 elevation in the serum (data not shown), indicating another unknown mechanism underlying the mobilization of BM-MSCs from BM into circulation and damaged muscles.

Surface marker analyses have suggested the existence of multiple subpopulations in BM-MSCs [15, 16], and the roles of each population in vivo have remained unclear. Here, we demonstrated that BM-MSCs can be subdivided into $Lin^-/ckit^-/CD106^+/CD44^+$ and $Lin^-/ckit^-/CD106^+/CD44^-$ cells. Our whole-transcriptome analysis demonstrated that the $Lin^-/ckit^-/CD106^+/CD44^-$ cells preferentially expressed SDF-1α in BM. SDF-1α-expressing stromal cells in BM contribute to niche formation for HSCs [10, 13, 14, 45]. In addition, there are some similarities in the expression profiles of other genes between $Lin^-/ckit^-/CD106^+/CD44^-$ BMCs and CXCL12 (SDF-1α)-abundant reticular cells or niche-maintaining cells in BM [10–12, 14, 46]. From this context, we estimate that $Lin^-/ckit^-/CD106^+/CD44^-$ cells in BM may be involved in this niche formation mechanism for HSCs. Further precise investigations are necessary to elucidate the roles and functions of this mesenchymal cell population in BM.

Similar to HSC, heterogeneous MSC populations are also hierarchically organized at the apex, from stem-like cells with self-renewing capacity to more differentiated cells with limited lineage potentials [15, 16]. The stem cell populations in various tissues are generally thought to be in a slow cycling or quiescence state under physiological conditions [47–49]. In this study, the $Lin^-/ckit^-/CD106^+/CD44^+$ population was proliferative and dominantly accumulated in damaged muscles. Conversely, the $Lin^-/ckit^-/CD106^+/CD44^-$ population in BM was shown to be a slow-cycling population. Thus, it appears that the $Lin^-/ckit^-/CD106^+/CD44^+$ population includes effecter cells that egress into the circulation in response to injury and serve to support regeneration through their anti-inflammatory activity and resident stem-cell activation, whereas the $Lin^-/ckit^-/CD106^+/CD44^-$ population in BM includes a stem-like cell population. However, it is still unclear whether a hierarchical relationship between $Lin^-/ckit^-/$

$CD106^+/CD44^-$ and $Lin^-/ckit^-/CD106^+/CD44^+$ BMCs (Fig. 7) exists, and further studies are warranted to clarify the in vivo relationship of these two populations.

In a recent study, CD106 marked an MSC subpopulation with unique and powerful immunomodulatory activities in vitro [6]. However, no report is available for the in vivo function of $CD106^+$ MSCs. This study showed that recruited $Lin^-/ckit^-/CD106^+/CD44^+$ BMCs highly expressed TSG-6 in damaged muscle. TSG-6 is a strong anti-inflammatory protein that is secreted from MSCs in culture [3, 42, 50–52]. We also showed that the TSG-6- or TSG-6/CD44-mediated pathway activates myoblast and satellite cells in vitro and in vivo. In addition, we observed the acceleration of muscle regeneration as well as the suppression of inflammation following the treatment of freshly isolated $Lin^-/ckit^-/CD106^+/CD44^+$ BMCs, in part through the TSG-6-mediated pathway. However, we cannot yet determine the benefits of $Lin^-/ckit^-/CD106^+/CD44^-$ BMCs for damaged muscles. Although the accumulation of $Lin^-/ckit^-/CD106^+/CD44^-$ BMCs is low in mdx muscles, these cells may have a high impact on the muscle regeneration process. Therefore, in future studies, it would be of interest to investigate whether this small BM-MSCs fraction ($Lin^-/ckit^-/CD106^+/CD44^-$) has the same effect on muscle regeneration as observed in $Lin^-/ckit^-/CD106^+/CD44^+$ BMCs or whether they exhibit different activities, such as muscle differentiation.

In this study, we did not consider the potential effect of $Lin^-/ckit^-/CD106^+/CD44^+$ BMCs or TSG-6 on muscle resident fibro/adipocyte progenitors (FAPs). Recent studies have indicated that sufficient FAPs activities are important for muscle regeneration [53–55]. It is also known that BM-MSCs and FAPs have similar surface markers [54, 55] and express CD44 [56, 57], thus suggesting that TSG-6 secreted from $Lin^-/ckit^-/CD106^+/CD44^+$ BMCs also has effects on FAP proliferation and activities to facilitate muscle regeneration. The interaction of BM-MSCs with FAPs during muscle regeneration needs to be investigated precisely in the future. Together, these findings illustrate the putative scheme for the roles of the BM-derived $Lin^-/ckit^-/CD106^+/CD44^+$ BMCs, which dominantly migrate in damage muscles and release TSG-6, with other trophic factors, to suppress inflammation/fibrosis and promote muscle regeneration processes in vivo. With future studies, the local/systemic administration of TSG-6 may become a new candidate strategy for improving DMD pathology.

Conclusions

In conclusion, it is clear that the normalization of dystrophin gene expression is necessary for the ultimate cure of DMD. Nevertheless, we consider that the series of results shown here have a significant impact on the muscle repair mechanisms by the endogenous BM-MSC population. This study also provides a novel concept that the normalization of MSC populations in BM may prevent the secondary exacerbation of inflammatory/fibrotic damages and improve clinical manifestations. A chronic exhaustion of MSC populations in BM appears to occur in other intractable hereditary or nonhereditary diseases besides DMD if persistent injury and inflammation continuously activate $Lin^-/ckit^-/CD106^+/CD44^+$ cells in BM. Further precise analyses of heterogeneous BM-MSC populations to understand their roles and mechanisms in various in vivo pathological settings may provide novel therapeutic strategies by targeting intrinsic homeostatic maintenance mechanisms driven by BM-MSCs in vivo.

Acknowledgments

R.F. was funded by a Research Fellowship (#243873) from the Japan Society for the Promotion of Science (JSPS), Japan. This study was also supported by a Grant-in-Aid for Scientific Research from the Ministry of Education, Culture, Sports, Science, and Technology of Japan and a Health and Labour Sciences Research Grant (Research of Intractable Diseases) from the Ministry of Health, Labour, and Welfare of Japan.

Author Contributions

R.F.: conception and design, performed experiments, collection and/or assembly of data, data analysis and interpretation, financial support, and manuscript writing; K.T.: conception and design, manuscript writing, financial support, and final approval of manuscript; E.A.: collection and/or assembly of data and data analysis and interpretation; K.N. and S.I.: data analysis and interpretation; Y. Kikuchi: administrative support and provision of study material; Y. Kaneda: conception and design, financial support, and final approval of manuscript.

Disclosure of Potential Conflicts of Interest

The authors indicate no potential conflicts of interest.

References

1 Pittenger MF, Mackay AM, Beck SC et al. Multilineage potential of adult human mesenchymal stem cells. Science 1999;284:143–147.

2 Prockop DJ. Marrow stromal cells as stem cells for nonhematopoietic tissues. Science 1997;276:71–74.

3 Lee RH, Pulin AA, Seo MJ et al. Intravenous hMSCs improve myocardial infarction in mice because cells embolized in lung are activated to secrete the anti-inflammatory protein TSG-6. Cell Stem Cell 2009;5:54–63.

4 Gupta N, Su X, Popov B et al. Intrapulmonary delivery of bone marrow-derived mesenchymal stem cells improves survival and attenuates endotoxin-induced acute lung injury in mice. J Immunol 2007;179:1855–1863.

5 Wu Y, Chen L, Scott PG et al. Mesenchymal stem cells enhance wound healing through differentiation and angiogenesis. StemCells 2007;25:2648–2659.

6 Yang ZX, Han ZB, Ji YR et al. CD106 identifies a subpopulation of mesenchymal stem cells with unique immunomodulatory properties. PLoS One 2013;8:e59354.

7 Otsuru S, Tamai K, Yamazaki T et al. Bone marrow-derived osteoblast progenitor cells in circulating blood contribute to ectopic bone formation in mice. Biochem Biophys Res Commun 2007;354:453–458.

8 Otsuru S, Tamai K, Yamazaki T et al. Circulating bone marrow-derived osteoblast progenitor cells are recruited to the bone-forming site by the CXCR4/stromal cell-derived factor-1 pathway. StemCells 2008;26:223–234.

9 Tamai K, Yamazaki T, Chino T et al. PDGFRalpha-positive cells in bone marrow are mobilized by high mobility group box 1 (HMGB1) to regenerate injured epithelia. Proc Natl Acad Sci USA 2011;108:6609–6614.

10 Sugiyama T, Kohara H, Noda M et al. Maintenance of the hematopoietic stem cell pool by CXCL12-CXCR4 chemokine signaling in bone marrow stromal cell niches. Immunity 2006;25:977–988.

11 Ding L, Morrison SJ. Haematopoietic stem cells and early lymphoid progenitors occupy distinct bone marrow niches. Nature 2013;495:231–235.
12 Ding L, Saunders TL, Enikolopov G et al. Endothelial and perivascular cells maintain haematopoietic stem cells. Nature 2012;481: 457–462.
13 Greenbaum A, Hsu YM, Day RB et al. CXCL12 in early mesenchymal progenitors is required for haematopoietic stem-cell maintenance. Nature 2013;495:227–230.
14 Morrison SJ, Scadden DT. The bone marrow niche for haematopoietic stem cells. Nature 2014;505:327–334.
15 Anjos-Afonso F, Bonnet D. Nonhematopoietic/endothelial SSEA-1+ cells define the most primitive progenitors in the adult murine bone marrow mesenchymal compartment. Blood 2007;109:1298–1306.
16 Sarugaser R, Hanoun L, Keating A et al. Human mesenchymal stem cells self-renew and differentiate according to a deterministic hierarchy. PLoS One 2009;4:e6498.
17 Qian H, Badaloni A, Chiara F et al. Molecular characterization of prospectively isolated multipotent mesenchymal progenitors provides new insight into the cellular identity of mesenchymal stem cells in mouse bone marrow. Mol Cell Biol 2013;33:661–677.
18 Qian H, Le Blanc K, Sigvardsson M. Primary mesenchymal stem and progenitor cells from bone marrow lack expression of CD44 protein. J Biol Chem 2012;287:25795–25807.
19 Sicinski P, Geng Y, Ryder-Cook AS et al. The molecular basis of muscular dystrophy in the mdx mouse: A point mutation. Science 1989;244:1578–1580.
20 Miyagoe-Suzuki Y, Takeda S. Gene therapy for muscle disease. Exp Cell Res 2010; 316:3087–3092.
21 Blake DJ, Weir A, Newey SE et al. Function and genetics of dystrophin and dystrophin-related proteins in muscle. Physiol Rev 2002;82:291–329.
22 Partridge TA, Morgan JE, Coulton GR et al. Conversion of mdx myofibres from dystrophin-negative to -positive by injection of normal myoblasts. Nature 1989;337:176–179.
23 Skuk D, Paradis M, Goulet M et al. Intramuscular transplantation of human postnatal myoblasts generates functional donor-derived satellite cells. Mol Ther 2010;18:1689–1697.
24 Sampaolesi M, Blot S, D'Antona G et al. Mesoangioblast stem cells ameliorate muscle function in dystrophic dogs. Nature 2006; 444:574–579.
25 Darabi R, Gehlbach K, Bachoo RM et al. Functional skeletal muscle regeneration from differentiating embryonic stem cells. Nat Med 2008;14:134–143.
26 Darabi R, Arpke RW, Irion S et al. Human ES- and iPS-derived myogenic progenitors restore DYSTROPHIN and improve contractility upon transplantation in dystrophic mice. Cell Stem Cell 2012;10:610–619.
27 Percival JM, Whitehead NP, Adams ME et al. Sildenafil reduces respiratory muscle weakness and fibrosis in the mdx mouse model of Duchenne muscular dystrophy. J Pathol 2012;228:77–87.
28 Gehrig SM, van der Poel C, Sayer TA et al. Hsp72 preserves muscle function and slows progression of severe muscular dystrophy. Nature 2012;484:394–398.
29 Ono Y, Calhabeu F, Morgan JE et al. BMP signalling permits population expansion by preventing premature myogenic differentiation in muscle satellite cells. Cell Death Differ 2011;18:222–234.
30 Musaro A, Barberi L. Isolation and culture of mouse satellite cells. Methods Mol Biol 2010;633:101–111.
31 Franken NA, Rodermond HM, Stap J et al. Clonogenic assay of cells in vitro. Nat Protoc 2006;1:2315–2319.
32 Fujita R, Kawano F, Ohira T et al. Anti-interleukin-6 receptor antibody (MR16-1) promotes muscle regeneration via modulation of gene expressions in infiltrated macrophages. Biochim Biophys Acta 2014;1840: 3170–3180.
33 Mori M, Nakagami H, Rodriguez-Araujo G et al. Essential role for miR-196a in brown adipogenesis of white fat progenitor cells. PLoS Biol 2012;10:e1001314.
34 Trapnell C, Williams BA, Pertea G et al. Transcript assembly and quantification by RNA-Seq reveals unannotated transcripts and isoform switching during cell differentiation. Nat Biotechnol 2010;28:511–515.
35 Trapnell C, Roberts A, Goff L et al. Differential gene and transcript expression analysis of RNA-seq experiments with TopHat and Cufflinks. Nat Protoc 2012;7:562–578.
36 Huang da W, Sherman BT, Lempicki RA. Systematic and integrative analysis of large gene lists using DAVID bioinformatics resources. Nat Protoc 2009;4:44–57.
37 Huang da W, Sherman BT, Lempicki RA. Bioinformatics enrichment tools: Paths toward the comprehensive functional analysis of large gene lists. Nucleic Acids Res 2009;37:1–13.
38 Nakamura A, Takeda S. Mammalian models of Duchenne muscular dystrophy: Pathological characteristics and therapeutic applications. J Biomed Biotechnol 2011;2011: 184393.
39 Morikawa S, Mabuchi Y, Kubota Y et al. Prospective identification, isolation, and systemic transplantation of multipotent mesenchymal stem cells in murine bone marrow. J Exp Med 2009;206:2483–2496.
40 Morikawa S, Mabuchi Y, Niibe K et al. Development of mesenchymal stem cells partially originate from the neural crest. Biochem Biophys Res Commun 2009;379:1114–1119.
41 Coutu DL, Francois M, Galipeau J. Inhibition of cellular senescence by developmentally regulated FGF receptors in mesenchymal stem cells. Blood 2011;117: 6801–6812.
42 Oh JY, Roddy GW, Choi Het al. Anti-inflammatory protein TSG-6 reduces inflammatory damage to the cornea following chemical and mechanical injury. Proc Natl Acad Sci USA 2010;107:16875–16880.
43 Hagiwara H, Ohsawa Y, Asakura S et al. Bone marrow transplantation improves outcome in a mouse model of congenital muscular dystrophy. FEBS Lett 2006;580:4463–4468.
44 Koning JJ, Kooij G, de Vries HE et al. Mesenchymal stem cells are mobilized from the bone marrow during inflammation. Front Immunol 2013;4:49.
45 Mendez-Ferrer S, Michurina TV, Ferraro F et al. Mesenchymal and haematopoietic stem cells form a unique bone marrow niche. Nature 2010;466:829–834.
46 Omatsu Y, Seike M, Sugiyama T et al. Foxc1 is a critical regulator of haematopoietic stem/progenitor cell niche formation. Nature 2014;508:536–540.
47 Arai F, Hirao A, Ohmura M et al. Tie2/angiopoietin-1 signaling regulates hematopoietic stem cell quiescence in the bone marrow niche. Cell 2004;118:149–161.
48 Kubota Y, Takubo K, Suda T. Bone marrow long label-retaining cells reside in the sinusoidal hypoxic niche. Biochem Biophys Res Commun 2008;366:335–339.
49 Ono Y, Masuda S, Nam HS et al. Slow-dividing satellite cells retain long-term self-renewal ability in adult muscle. J Cell Sci 2012;125:1309–1317.
50 Lee TH, Wisniewski HG, Vilcek J. A novel secretory tumor necrosis factor-inducible protein (TSG-6) is a member of the family of hyaluronate binding proteins, closely related to the adhesion receptor CD44. J Cell Biol 1992;116:545–557.
51 Milner CM, Higman VA, Day AJ. TSG-6: A pluripotent inflammatory mediator? Biochem Soc Trans 2006;34:446–450.
52 Wisniewski HG, Vilcek J. Cytokine-induced gene expression at the crossroads of innate immunity, inflammation and fertility: TSG-6 and PTX3/TSG-14. Cytokine Growth Factor Rev 2004;15:129–146.
53 Heredia JE, Mukundan L, Chen FM et al. Type 2 innate signals stimulate fibro/adipogenic progenitors to facilitate muscle regeneration. Cell 2013;153:376–388.
54 Joe AW, Yi L, Natarajan A et al. Muscle injury activates resident fibro/adipogenic progenitors that facilitate myogenesis. Nat Cell Biol 2010;12:153–163.
55 Uezumi A, Fukada S, Yamamoto N et al. Mesenchymal progenitors distinct from satellite cells contribute to ectopic fat cell formation in skeletal muscle. Nat Cell Biol 2010;12: 143–152.
56 Pisani DF, Clement N, Loubat A et al. Hierarchization of myogenic and adipogenic progenitors within human skeletal muscle. StemCells 2010;28:2182–2194.
57 Wosczyna MN, Biswas AA, Cogswell CA et al. Multipotent progenitors resident in the skeletal muscle interstitium exhibit robust BMP-dependent osteogenic activity and mediate heterotopic ossification. J Bone Miner Res 2012;27:1004–1017.

ORIGINAL ARTICLE

See related commentary on pg 302

Dynamic Analysis of Histamine-Mediated Attenuation of Acetylcholine-Induced Sweating via GSK3β Activation

Saki Matsui[1], Hiroyuki Murota[1], Aya Takahashi[1], Lingli Yang[1], Jeong-Beom Lee[2], Kouta Omiya[3], Masato Ohmi[3], Junichi Kikuta[4], Masaru Ishii[4] and Ichiro Katayama[1]

Sweating has been associated with the exacerbation of atopic dermatitis (AD) in diverse ways. Acetylcholine (ACh)-mediated sweating is known to be attenuated in AD, but its cause remains obscure. To address this issue, the impact of histamine on ACh-induced sweating was evaluated. Sweating was measured by counting the number of active sweat pores by the starch–iodine reaction and dynamic optical coherence tomography; sweat was visualized using two-photon excitation fluorescence microscopy in mice and the quantitative sudomotor axon reflex test in humans. Both histamine receptor antagonists and H1 receptor (H1R)-knockout (KO) mice were used to determine methodological specificity. Histamine demonstrably inhibited ACh-induced sweating in both mice and humans via H1R-mediated signaling. In sweat glands, ACh inactivated glycogen synthase kinase 3β (GSK3β), a kinase involved in endocytosis and secretion, whereas simultaneous stimulation with histamine activated GSK3β. Results of two-photon excitation fluorescence microscopy confirmed the dynamic motion of sweat and sweat glands after ACh treatment, showing that simultaneous stimulation with histamine altered their dynamic properties. These results indicate that histamine inhibits sweat gland secretions by blocking ACh-induced inactivation of GSK3β. Histamine-mediated hypohidrosis might be involved in the mechanism of abnormal skin dryness in patients with AD.

Journal of Investigative Dermatology (2014) **134,** 326–334; doi:10.1038/jid.2013.323; published online 29 August 2013

INTRODUCTION

Disturbances in the homeostatic function of the skin evoke a variety of dermatoses. Sweating is involved in the maintenance of skin homeostasis, with antimicrobial (Rieg *et al*, 2005; Schittek *et al*, 2008) and moisturizing effects (Eishi *et al*, 2002), and in the regulation of skin surface pH (Schmid-Wendtner and Korting, 2006). Recent reports also suggest that impaired sudomotor function contributes to the pathogenesis of atopic dermatitis (AD) (Imayama *et al*, 1994; Eishi *et al*, 2002; Kitaba *et al*, 2011; Shiohara *et al*, 2011; Kijima *et al*, 2012), and agree that deterioration of sudomotor function is found in patients with AD. These results indicate that reduction of sweating might impair moisturization and protection against infections of the skin. However, the mechanism of aberrant sweating in AD remains unknown.

There are likely two hypotheses: the first is sweat duct obstruction by abnormal keratinization (Sulzberger *et al*, 1947; Papa and Kligman, 1966) and the second is abnormal sudomotor function of sweat glands (Kijima *et al*, 2012). Because not all AD patients with anhidrosis develop histopathological sweat duct obstruction, we hypothesize that certain inflammatory mediators might reduce the function of sweat glands. A potential candidate for this hypothesis was histamine, which signals through a seven-transmembrane receptor, as well as an acetylcholine (ACh) receptor (Du Buske, 1996; Simons and Simons, 2011). It is well known that antihistamines also have anticholinergic properties (Meltzer, 1990; Du Buske, 1996; Murota and Katayama, 2011). Thus, we evaluated the effects of histamine on ACh-mediated sweating in animals.

Assessment of sudomotor function varies in methodology and has been evaluated by visualization of the sweat response by the iodine–starch reaction (Nejsum *et al*, 2002) or optical coherence tomography (OCT) (Ohmi *et al*, 2009).

Here, we evaluated the impact of histamine on ACh-mediated sweating using a multimodal approach *in vivo*, and discuss the possible involvement of sudomotor dysfunction. Moreover, in this study, we attempted to visualize the sweat response using two-photon excitation fluorescence

[1]*Department of Dermatology, Course of Integrated Medicine, Graduate School of Medicine, Osaka University, Osaka, Japan;* [2]*Department of Physiology, College of Medicine, Soonchunhyang University, Chenan, Republic of Korea;* [3]*Course of Health Science, Graduate School of Medicine, Osaka University, Osaka, Japan and* [4]*Laboratory of Cellular Dynamics, WPI-Immunology Frontier Research Center, Osaka University, Osaka, Japan*

Correspondence: Hiroyuki Murota, Department of Dermatology, Course of Integrated Medicine, Graduate School of Medicine, Osaka University, 2-2 Yamadaoka, Suita, Osaka 5650871 Japan.
E-mail: h-murota@derma.med.osaka-u.ac.jp

Abbreviations: ACh, acetylcholine; AD, atopic dermatitis; ANOVA, analysis of variance; GSK3α/β, glycogen synthase kinase 3α/β; H1R, histamine type-1 receptor; KO, knockout; M3R, muscarinic 3 receptor; OCT, optical coherence tomography; QSART, quantitative sudomotor axon reflex test

Received 31 March 2013; revised 29 May 2013; accepted 29 May 2013; accepted article preview online 30 July 2013; published online 29 August 2013

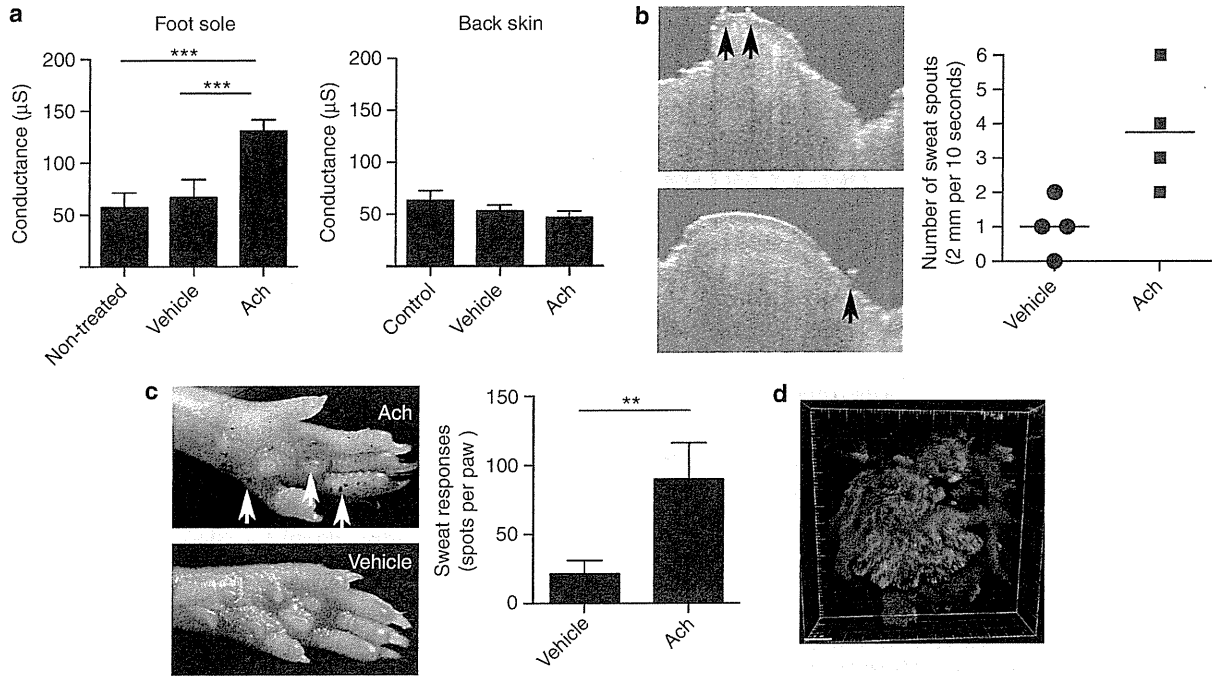

Figure 1. Multimodal approach to assess sudomotor response to acetylcholine (Ach) *in vivo*. (**a**) The degree of stratum corneum hydration was assessed with conductance measurements. Left: foot sole, right: back skin. Statistical analysis was performed by one-way analysis of variance, Bonferroni's multiple comparison test ($n = 5$–6). (**b**) Dynamic images of sweating visualized by optical coherence tomography. Graph data show the quantification of the images ($n = 5$). (**c**) The result of counting the number of iodine–starch reaction–positive sweat pores. $^{**}P = 0.003$, unpaired *t*-test ($n = 5$–7). Arrows indicate the positive spots. (**d**) Observations with two-photon microscopic analysis allowed a complete view of sweat glands. Green (FITC): gross cystic disease fluid protein (sweat gland); red (Texas Red): dextran (microvessels).

microscopy and succeeded in obtaining the dynamic images of sweat glands after sudomotor stimulation.

RESULTS

Validation of evaluation methodologies for ACh-mediated sweating in mice

To demonstrate the validity of assessment of sudomotor function in mice, four different methods were performed. First, skin hydration was evaluated by the impedance method based on the idea that sweat will moisten the skin surface (Figure 1a). Skin hydration significantly increased on the ACh-treated foot sole, but not on ACh-treated, sweat gland–free back skin. The dynamic image of sweating obtained by OCT revealed the increased sweat spout from the sweat duct on the ACh-treated foot sole (Figure 1b and Supplementary Figure 1 online). The sudomotor reaction to ACh was also confirmed by counting the number of iodine–starch reaction–positive sweat pores (Figure 1c). These results indicate that our multimodal evaluations can adequately assess the sudomotor reaction to ACh *in vivo*. Furthermore, two-photon microscopic analysis revealed the three-dimensional structures of sweat glands and microvessels visualized using anti-gross cystic disease fluid protein antibody and intravenously administered red fluorescent dextran, respectively (Figure 1d).

Effects of histamine on ACh-mediated sudomotor function

Histamine was administered simultaneously with ACh, and sudomotor response was examined in mice. First, the measurement results of skin hydration were increased by stimulation with ACh alone, but there was no apparent increase after coadministration of histamine with ACh (Figure 2a). In the observation record of OCT, the number of active sweat glands in ACh-treated mice decreased after coadministration of histamine (Supplementary Figure 1B and C online). High numbers of sweat pores positive for the iodine–starch reaction by ACh treatment decreased after coadministration of histamine (Figure 2b). To confirm which type of histamine receptor has a crucial role in the suppression of sudomotor function, antagonists for histamine receptors (i.e., H1 receptor (H1R), H2R, and H4R) were administered intraperitoneally (Figure 2b). Pyrilamine and fexofenadine, H1R antagonists, decreased the ACh-induced sweating response and prevented the histamine-mediated inhibition of ACh-induced sweating. In contrast, both H2 and H4 receptor antagonists markedly reduced ACh-induced sweating, but did not affect the histamine-mediated inhibition of ACh-induced sweating (Figure 2b). H1R-knockout (KO) mice showed no apparent inhibition by histamine of increased skin hydration (Figure 2c) and of increased number of iodine–starch reaction–positive sweat pores by Ach treatment (Figure 2d).

Localization of ACh and histamine receptors in the microenvironment of the eccrine sweat gland

Next, to resolve the question of the unknown mechanism of histamine-mediated inhibition of sweating, the localization of

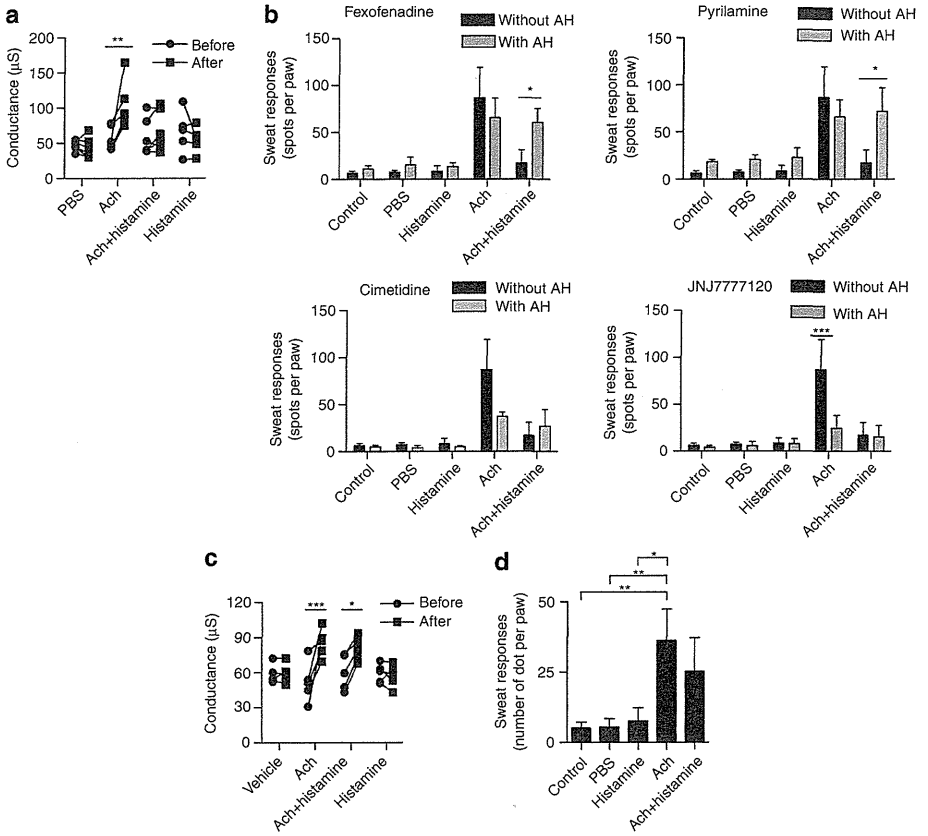

Figure 2. The effects of histamine (His) on sudomotor function. (**a**) The degree of stratum corneum hydration was assessed with conductance measurements before (black circles) and after (black square) acetylcholine (Ach) administration with or without His. $^{**}P<0.01$, two-way analysis of variance (ANOVA), Bonferroni's multiple comparison test ($n=5$–6). (**b**) The result of counting the number of iodine–starch reaction–positive sweat pores with or without administration of various antihistamines. Antagonists for H1R, H2R, and H4R were fexofenadine or pyrilamine, cimetidine, and JNJ7777120, respectively. AH, antihistamine. $^{***}P<0.001$, $^{*}P<0.05$, two-way ANOVA, Bonferroni's multiple comparison test ($n=5$–7). (**c**) The degree of stratum corneum hydration in H1R-KO mice was assessed with conductance measurements before (black circles) and after (black square) Ach with or without His. $^{***}P<0.001$, $^{*}P<0.05$, two-way ANOVA, Bonferroni's multiple comparison test ($n=5$). (**d**) The results of counting the number of iodine–starch reaction–positive sweat pores in H1R-KO mice. $^{**}P<0.01$, $^{*}P<0.05$, one-way ANOVA, Bonferroni's multiple comparison test ($n=5$–6).

histamine or ACh receptors in the microenvironment of the sweat gland was determined by immunohistochemical staining (Figure 3 and Table 1). The muscarinic 3 receptor (M3R) was chosen as the ACh receptor, because ACh receptors in mouse eccrine sweat glands are predominantly M3R (Vilches *et al*, 1995). As a result, sweat glands expressed H1, H2, H4 and M3 receptors. Protein gene product-9.5-positive peripheral nerve fibers were co-stained with antibody against the H1, H2, and M3 receptors, but myoepithelial cells did not stain with antibodies against the H1, H2, H4, and M3 receptors. These results suggest that there might be cross talk between two distinct pathways downstream of histamine and ACh receptors in sweat glands and nerve fibers.

Histamine blocks phosphorylation of glycogen synthase kinase 3β activated by ACh stimulation

A phosphorylation antibody array using whole-skin lysates was used to examine the extent of cross talk between the histamine and ACh signaling pathways (Figure 4a). We found two candidate signal transducers, including glycogen synthase kinase 3α/β (GSK3α/β) and AMP-activated protein kinase α1, which were differentially phosphorylated by ACh and histamine treatment (Figure 4a). GSK3α/β and AMP-activated protein kinase α1 were phosphorylated by ACh alone, but not by ACh plus histamine or histamine alone. Among these molecules, we focused on GSK3β, which is thought to be involved in cellular membrane transport and trafficking (Adachi *et al*, 2009, Rexhepaj *et al*, 2010). Such phosphorylation dynamics of GSK3β were also observed in western blotting analysis (Figure 4b). Immunohistochemical staining of phosphorylated GSK3β was performed to confirm whether this cross talk occurred in eccrine sweat glands. As a result, phosphorylation of GSK3β was observed in sweat glands of ACh-treated skin, but not in ACh- and histamine-treated skin (Figure 4c).

Histamine reduces the frequency of sweat secretion

As GSK3β is inactivated by phosphorylation, the adiaphoretic effect of histamine was assumed to be due to decreased

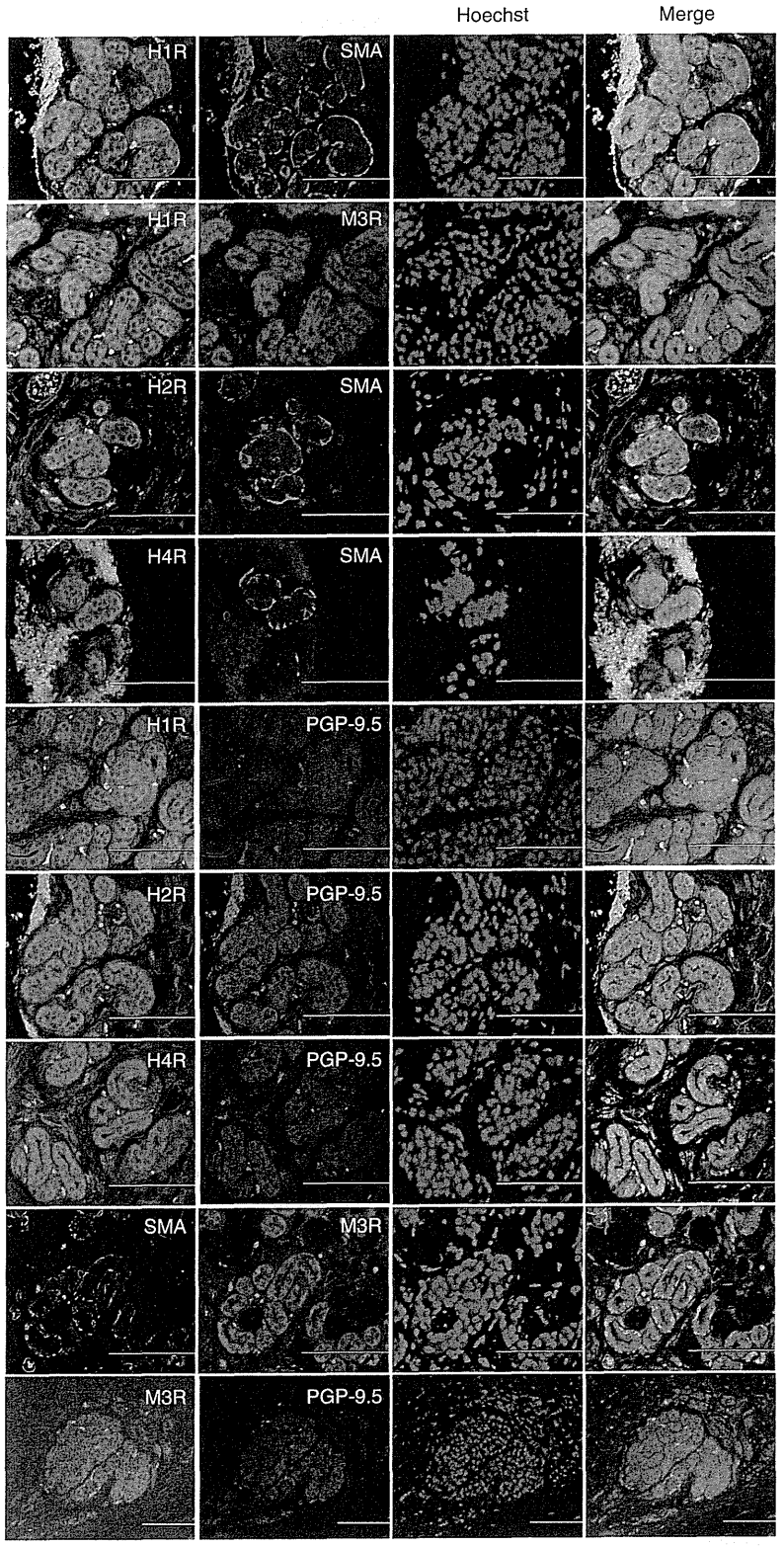

Figure 3. Localization of H1, H2, H4, and M3 receptors in the sweat gland microenvironment. Skin specimens derived from mice hindpaws were immunohistochemically stained with antibodies against histamine receptors, SMA, protein gene product-9.5 (PGP-9.5), and M3 receptor. Bar = 100 μm.

secretion of sweat by activation of GSK3β. To confirm this hypothesis, the dynamic imaging of sweat glands in mouse hindpaws was observed using two-photon microscopy. In this attempt, three-dimensional images of sweat glands and their configuration were obtained. After 15 minutes of intraperitoneal ACh administration, the sweat glands became distended and contracted, followed by the appearance of optically less-transparent areas, seen as 'dark' spots (Figure 5a and b and Supplementary Figures 2A, B and 3A online). Although we could not definitely identify the entity of the opaque spots, we reasonably assumed that these spots are derived from the change in local pH, that is, acidification due to sweating (fluorescent intensity of fluorescein is known to be critically dependent on the pH of the environment (Ohkuma and Poole, 1978)).

In contrast to ACh administration, simultaneous intraperitoneal administration of histamine decreased the number of opaque spots (Figure 5a–c and Supplementary Figures 2C and 3B online).

Table 1. Localization of H1R, H2R, H4R, and M3R on eccrine sweat gland

	H1R	H2R	H4R	M3R
Sweat gland	+	+	+	+
Myoepithelial cell	–	–	–	–
Nerve fiber	+	+	–	+

Abbreviations: H1, 2, and 4R, type 1, 2, and 4 histamine receptor, respectively; M3R, muscarinic 3 receptor.

Histamine decreases the ACh-induced, axon reflex–mediated sweating volume in humans

The inhibitory effects of histamine on ACh-mediated sweating in humans were assessed by quantitative sudomotor axon reflex test (QSART) (Figure 6). When histamine was iontophoretically applied with ACh simultaneously, QSART-measured results were significantly decreased compared with results from stimulation solely with ACh.

DISCUSSION

The present study has partly revealed the mechanisms of anhidrosis in AD using multiple assessments, showing that the inhibitory effect of histamine on Ach-induced sweating occurred via phosphorylation (inactivation) of GSK3β downstream of the H1R.

First, it was surprising that histamine has effects other than induction of allergic inflammation. It has been reported that histamine affects many kinds of cells, which express histamine

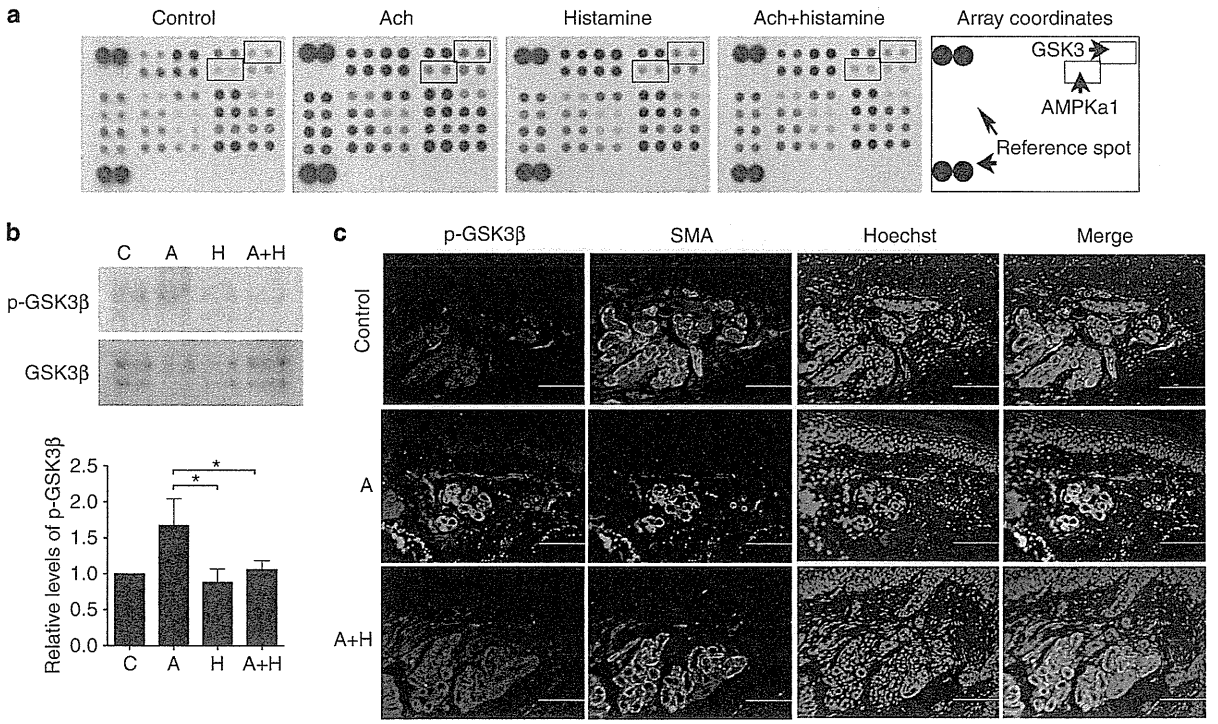

Figure 4. Cross talk between acetylcholine (Ach)- and histamine-mediated signal transduction. (**a**) Phosphorylation profiles of kinases and protein substrates in Ach- or His-treated skin were analyzed with a phosphokinase antibody array. (**b**) Western blot analysis for phosphorylated GSK3β (p-GSK3β) and GSK3β. The graph shows the relative levels of p-GSK3β (mean ± SD). Signal intensity was determined by densitometry. Relative phosphorylation was calculated and normalized against total amounts of GSK3β and quantified against the signal intensity of the control group. *$P<0.05$, two-way analysis of variance, Bonferroni's multiple comparison test ($n=3$). A, acetylcholine; A + H, acetylcholine + histamine; C, control; H, histamine. (**c**) Skin specimens derived from hindpaws stimulated with ACh with or without histamine were immunohistochemically stained with anti-p-GSK3β and anti-SMA antibodies. Bar = 100 μm.

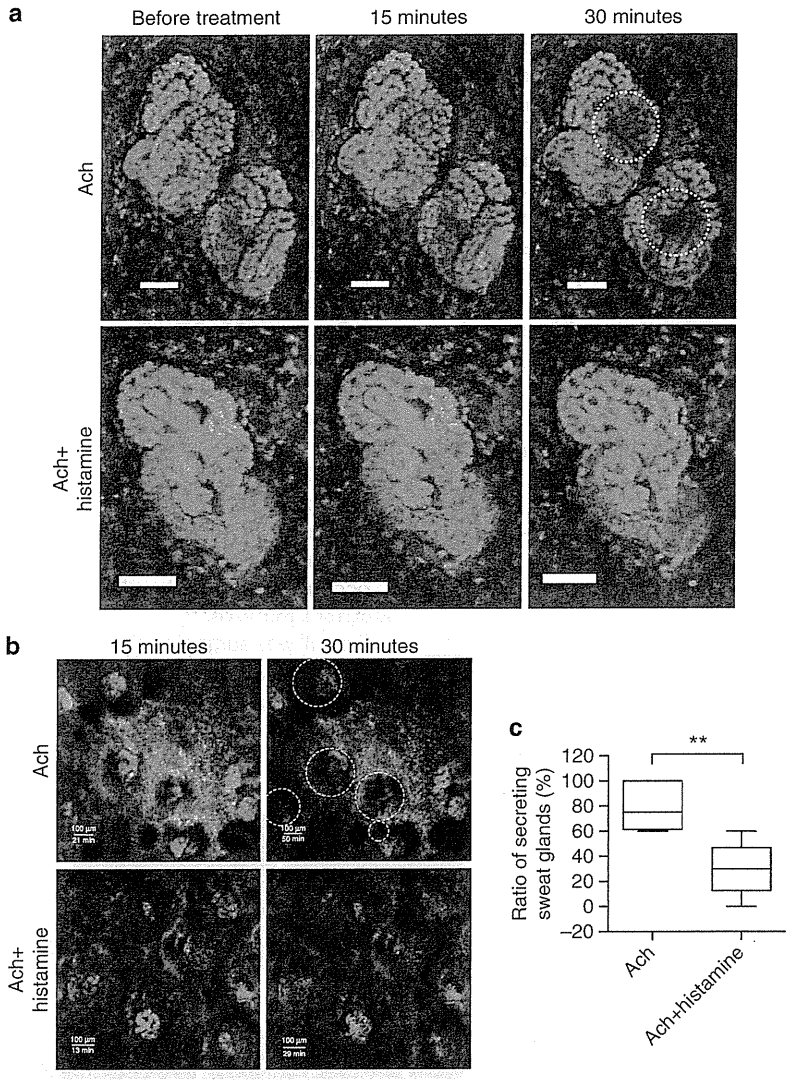

Figure 5. Dynamic imaging of sweat glands by two-photon microscopic analysis. (**a**) Acetylcholine (ACh) or ACh and histamine (ACh + histamine) were intraperitoneally injected. Subsequently, the motion of the sweat glands was recorded for 30 minutes. Photos before treatment, 15 minutes, and 30 minutes after observation are presented. Circles with a dotted line show the opaque spots that possibly suggest sweating. Bar = 50 μm. (**b**) The number of low-density spots per field per 30 minutes was counted. Bar = 500 μm. Circles with a dotted line enclose the low-density spots. (**c**) The ratio of the number of sweat glands associated with or without low-density spots is presented. $^{**}P<0.01$, unpaired *t*-test ($n=5$).

receptors. Previous studies also revealed that histamine is involved in (1) waking mechanisms (Lin *et al*, 1988), cognitive functioning (Gengo and Manning, 1990), and regulating the level of food intake by affecting neuronal activity (Masaki *et al*, 2004); (2) innate immune responses (Ertam *et al*, 2007; Metz *et al*, 2011); and (3) induction of chemokines, cytokines, and adhesion molecules on various types of cells (Fujikura *et al*, 2001; Giustizieri *et al*, 2004; Murota and Katayama, 2011). However, as far as we know, the effects of histamine on the sweating response have not been reported.

Recent reports shed light on the possible involvement of decreased sweating in the pathogenesis of AD (Eishi *et al*, 2002; Shiohara *et al*, 2011; Kijima *et al*, 2012; Sugawara *et al*, 2012), but the mechanisms of hypohidrosis in AD remain obscure. The pathogenic involvement of histamine in AD has been discussed in past articles, as histamine was thought to contribute to early events in AD (Akdis *et al*, 2006; Vanbervliet *et al*, 2011). The results of our study suggest that histamine might also impair skin homeostasis via decreasing sweating volume. Decreased sweating is also found in patients with urticaria, especially the cholinergic type (Itakura *et al*, 2000; Kobayashi *et al*, 2002). Thus, it might be said that sweating dysfunction may contribute to histamine-related skin disorders.

Furthermore, we found that H1Rs had a crucial role in histamine-mediated inhibition of ACh-induced sweating. Administration of H1R antagonists in wild-type mice attenuated the inhibitory effects of histamine on ACh-induced